12-2011

An Investigation of the Application of Phase Change Materials in Practical Thermal Management Systems

David Ewing
Clemson University, dewing@clemson.edu

Recommended Citation

Ewing, David, "An Investigation of the Application of Phase Change Materials in Practical Thermal Management Systems" (2011). *All Dissertations*. 820.
https://tigerprints.clemson.edu/all_dissertations/820

An Investigation of the Application of Phase Change Materials in Practical Thermal Management Systems

A Dissertation
Presented to
the Graduate School of
Clemson University

In Partial Fulfillment
of the Requirements for the Degree
Doctor of Philosophy
Mechanical Engineering

---

by
David Ewing
December 2011

Committee Members:
Lin Ma, Committee Chair
Donald Beasley
Richard Miller
Chenning Tong

Abstract

This work investigates the application of alternative cooling techniques to thermal management. In the first section, this work presents models and extensive simulation studies on an alternative cooling strategy based upon phase change materials (PCMs) for the thermal management system of a LED headlight assembly. These studies have shown that properly chosen PCMs, when suspended in metal foam matrices, increased the thermal conductivity of the PCM. The increased thermal conductivity can enhance the cooling characteristics of a practical thermal management system for a LED headlight system. To further enhance the advantages of using PCMs, nanoparticle enhanced fluids (nanofluids) are desirable as an additional source of cooling. The use of nanofluids motivates the development of a new diagnostic tool for multiphase flows and a minimization algorithm for analyzing the data. For this purpose, the second section of this work develops a new technique that is based on wavelength-multiplexed laser extinction (WMLE) to measure particle sizes in multiphase flows. In the final section of this work, the simulated algorithm (SA) is investigated for analyzing the data collected in this work. Specifically, the parallelization of the SA technique is investigated to reduce the high computational cost associated with the SA algorithm.

Acknowledgements

I owe my deepest gratitude to my supervisor, Dr. Lin Ma, for without his advice and leadership this work would not be possible. His encouragement, guidance and support are greatly appreciated. I would also like to thank Drs. Richard Miller, Donald Beasley and Chenning Tong for serving on my advisory committee.

In addition, I would thank all of my colleagues in Dr. Ma's group; Dr. Weiwei Cai, Dr. Yan Zhao, and Xuesong Li. I will always gratefully remember their discussions of research and other subjects. I would also like to express my gratitude to my colleagues in the Department of Mechanical Engineering, including Dr. Todd Schweisinger, my fellow TAs, friends, and the staff. All of these people that I gladly call my friends have made my life in graduate school much more enjoyable, and I will be eternally grateful for their professional wisdom and friendship.

Most importantly, I am thankful for the support, both financially as well as emotionally, that I have received from my parents, sister, and many other friends. This work would not have been possible without them, and I will always remember the sacrifices each of them made for me.

Table of Contents

List of Tables

List of Figures

Chapter 1: Introduction

1.1 Motivation

The increased power demands in electric vehicles, especially when considering the vehicles' components, have hindered the progress of these vehicles. These increased demands are especially difficult when considering the limited battery power available in electric vehicles. Considering this limitation, many vehicle manufacturers are seeking to decrease the overall power demand of each vehicle component, such as by using light emitting diodes (LEDs) for their headlight systems. However, these new systems require increased thermal protection, especially in outdoor environments. These increased cooling needs demand more power for their individual thermal management systems. Since this power is at a premium in electric vehicles, a method to thermally protect these headlight systems is desired that requires little to no additional power draw for the thermal management system. This thermal management system must be capable of adequately cooling these component systems while maintaining packaging flexibility and reliable operation in many environments.

Therefore, this investigation first explores the concept of adding a phase change material (PCM) based heat sink for a LED headlight assembly. This strategy will utilize the PCM's natural phase change process in order to provide increased thermal protection for this component, while demanding no additional power from the electric vehicle's system.

To further enhance the favorable aspects of this PCM based heat sink, the application of nanoparticle suspended fluid (nanofluid) strategy is examined in this work. These nanofluids have been shown in the past to increase the heat transfer capabilities of the base fluid. The main challenge in accurately modeling this increase is that the sizing characteristics of these particles must be known. Therefore, a new diagnostic tool is needed for use in the study of multiphase flows. To address this issue, this work investigates a new methodology based on laser extinction to detect the sizing characteristics of particles in a multiphase flow. This methodology uses an optical process with multiple wavelengths to provide increased information to detect the sizing characteristics of the particles in multiphase flows.

One of the key issues in this methodology is the inversion process of the data in order to retrieve the sizing characteristics. Therefore, a new algorithm is desired to solve the inversion process to retrieve the sizing characteristics correctly. Therefore, the last portion of this investigation seeks to develop an inversion method based upon the simulated annealing (SA) algorithm. This inversion method, when implemented in a parallelized fashion, has been shown to be able to solve the problem with high fidelity, while reducing the normal computational cost of the SA algorithm.

1.2 Introduction to Phase Change Materials (PCMs)

PCMs have been extensively used in many engineering applications, including building materials for energy storage improvement [1, 2], energy storage systems [1, 2], electronics cooling systems [3-9], etc. One reason for the attractiveness of PCMs in such extensive applications is that, due to its latent heat property, a PCM essentially behaves as a thermal switch [10]. When the operation temperature of the target component increases to the melting temperature of the PCM, the temperature of the system will remain essentially steady until the PCM is completely melted. This phase change process enables the absorption of a large amount of heat without increasing the temperature of the electronic system being utilized. This process is a major consideration for choosing PCMs as an alternative cooling technique in this work.

Another important reason why a PCM-based cooling strategy is particularly attractive is the fact that the implementation of a particular PCM is relatively straightforward. A PCM can easily be implemented into an existing thermal management system because the latent heat property of the PCM is a natural process that does not require any additional energy input from the system. Also, the PCM can be easily implemented as a simple thermal block into an existing cooling system to provide added thermal protection of critical components. For these reasons, the thermal properties of an applicable PCM make it an attractive supplement to factory installed cooling strategies.

Of important interest is the role that the thermal conductivity of the PCM plays in the cooling system's performance [10]. In particular, organic PCMs exhibit many qualities needed in component cooling, including high latent heat, non-corrosiveness, etc. [1, 2, 10], but they also exhibit a prohibitively low thermal conductivity [1, 2, 10] to be used in practical thermal management systems. To overcome this limitation of low thermal conductivity, it has been the focus of many recent research efforts**,** including this work, to suggest suspending these PCMs in a metal foam matrix [4, 11-14] in order to increase the effective thermal conductivity of the suspension. In conjunction with the increase of the thermal conductivity of the PCM based heat sink, an optimization process for the selection of the optimal porosity of the PCM utilized must be performed that considers both the increase in thermal conductivity and loss of latent heat of the PCM in order to provide the maximum operational time in any system. Considering these factors, this work not only will explore the applicability of using a PCM in a proposed thermal management system, but also will find the optimal volume fraction of the proposed PCM to be utilized for an LED lighting system.

1.3 Introduction to Wavelength-Multiplexed Laser Extinction

To increase the effectiveness of the favorable aspects of PCMs discussed in the previous section, a strategy implementing nanofluids is also considered because of their increased heat transfer characteristics. One of the limiting factors in the study of nanofluids is measuring the size characteristics of the nanoparticles within this multiphase flow application.

Many laser-based techniques have been attempted for this purpose in the past. Of the methods investigated thus far, techniques based on laser extinction are especially attractive because of their relative simplicity in implementation and data interpretation, capability to provide continuous measurement with fast time response, very limited requirement of optical access, and species specificity if wavelengths are well chosen.

With these factors in mind, this work investigates and develops a sensor for particle measurements in multiphase flows based on wavelength-multiplexed laser extinction (WMLE). The sensor developed in this work has the unique advantage of incorporating multiple laser sources to expand the sensing capability of the diagnostic. With this increased ability, this sensor technique not only monitors the particle size and concentration, but also the size distribution and aggregation of the particles.

1.4 Introduction to Temperature Parallel Simulated Annealing

In order to improve the method for obtaining the sizing characteristics of the nanoparticles within the base fluid of a nanofluid, a new inversion method for analyzing the data is needed. This work explores a new technique for this purpose by using the simulated annealing (SA) technique. The simulated annealing (SA) algorithm was first introduced in 1983 for solving combinatorial optimization problems [15]. Recently, many research efforts have been devoted to successfully demonstrating its use in solving both discrete [16, 17] and continuous optimization problems [18-23], revealing several critical advantages of the use of the SA algorithm over other optimization techniques. For example, the SA algorithm can optimize complicated problems with a large number of variables and numerous confusing local minima. In addition, the SA algorithm is insensitive to the initial guess, which is especially important when no *a priori* information about the solution is available. Because of these advantages, the SA algorithm shows great promise in solving the sizing characteristics of nanoparticles within a base fluid.

On the other hand, the disadvantages of the SA algorithm are also well-recognized. One of the primary disadvantages of the SA algorithm is its high computational cost [20, 23]. Many research efforts have focused on developing variants of the SA algorithm to reduce the computational cost [24-26] by either optimizing the annealing schedule [16, 27-30], or by parallelizing the SA algorithm [25, 31-34]. However, the optimization of the annealing schedule is usually problem-dependent [27, 28], and therefore limits the applicability of the results from these efforts. For the parallelization of the SA algorithm, convergence is not guaranteed, and the maximum speedup efficiency is very limited [33, 34].

Considering these limitations of the SA algorithm and the subsequent methods to overcome them, this work studies the application of the temperature parallel simulated annealing (TPSA) algorithm, which combines the well-established parallel tempering (or replica exchange) method [35, 36] and the SA algorithm [37]. The TPSA algorithm overcomes the above limitations by theoretically guaranteeing convergence; increasing the speedup of the parallelization process; and, because the TPSA optimization process occurs at constant temperature, not requiring an annealing schedule [25, 32, 38].

However, the limiting factor to the application of the TPSA algorithm is the fact that this algorithm has only been studied primarily on discrete functions in previous efforts [16, 32, 33, 37, 39]. Therefore, this work conducts a systematic study of the TPSA algorithm on continuous functions that would be applicable to the purpose of this work.

1.5 Objectives of Dissertation

The first objective of this work is to explore the application of PCMs to an existing thermal management system in order to ensure increased thermal protection of a LED headlight assembly. Our studies have found that the use of specific PCMs shows promising results in extending the operational time of these components, especially when used in conjunction with metal foam suspensions in order to increase the thermal conductivity of the PCM being used. Also, our results have potentially established a procedure to optimize the volume fraction of the PCM in order to optimize the operational time.

The next objective of this work is to develop an optical technique combined with an inversion method applicable to multiphase flow applications in order to obtain the sizing characteristics of nanoparticles within a nanofluid. The development of these two concepts will enable further understanding of the application of nanofluids to the thermal management system using PCMs. Our studies have demonstrated that the WMLE method can effectively measure the size of particles in multiphase environments. Furthermore, our studies have shown that the implementation of a new inversion algorithm based upon simulated annealing (SA) in a parallelization environment can analyze the data obtained accurately under acceptable computational cost.

This work is based upon the work completed and published in three peer-reviewed journal articles; therefore, the rest of this work is organized as follows. In Chapter 2, the journal article that explores the application of PCMs to a LED headlight system is presented. Chapter 3 contains the journal article that pursues the development of the WMLE method for measuring particle/droplet sizes. Then, Chapter 4 presents the journal article that develops the TPSA algorithm. The final chapter summarizes the work that is contained within this dissertation.

Chapter 2: Investigation of the Application of Phase Change Materials (PCM)

2.1 Abstract

Phase change materials (PCMs) are extensively used in many engineering areas for thermal management purposes. This paper investigated the application of PCMs for vehicular systems, especially for the thermal protection of vehicle lighting systems based on light emitting diodes (LEDs). Lighting systems based on LEDs offer many advantages, however, also pose a smaller margin of error for thermal management. This paper analyzed the combined use of PCMs with metal foam for cooling systems. The cooling performance was studied numerically under different porosity values of the metal foam, and different boundary conditions. The cooling performance was also compared to a solid metal sink system (SMS) and was found to offer several distinct cooling characteristics.

2.2 Nomenclature

b = half thickness of bump in hexagonal structure of metal foam

CMS = cooling management system

SMS = solid management system

T = temperature

T_M = melting temperature of PCM

T_S = solidus temperature of PCM

T_L = liquidus temperature of PCM

D = Diameter of CMS and SMS unit

H = height of CMS and SMS unit

h = convective heat transfer

Q = heat added to system

C_P = specific heat at constant pressure

C_{Peff} = combined effective specific heat of conductor and PCM

$(\rho C_P)_{MF}$ = (ρC_P) of the metal foam

$(\rho C_P)_{PCM}$ = (ρC_P) of the PCM

k = thermal conductivity

k_{MF} = thermal conductivity of the metal foam

k_s = thermal conductivity of solid metal foam

k_f= thermal conductivity of PCM at its respective solid or liquid phase

k_{PCM} = thermal conductivity of the PCM

k_{eff} = combined effective thermal conductivity of conductor and PCM

r = area ratio of the solid fiber to void area

h_{ref} = reference enthalpy

h_{sens}= sensible enthalpy

T_{ref} = reference temperature

L = latent heat

L_f = half length of fiber of metal foam

S_h = source term to correct the latent heat variation during the melting process

ΔH = heat of fusion

H_{tot} = total enthalpy of material

Δt = time step

FC = forced convection condition

NC = natural convection condition

AD = Adiabatic condition

Greek Symbols

ρ = density

ρ_{MF} = density of the metal foam

ρ_{PCM} = density of the PCM

ρ_{eff} = effective density

ε = volume fraction of the PCM

β = liquid fraction

2.3 Introduction

Phase change materials (PCMs) are extensively used in many engineering applications. They are used in energy storage systems [40], electronics cooling systems [41], building materials for energy storage improvement [42], heat exchangers [43], and many other similar applications. This paper investigated the applications of PCMs for the thermal management in vehicular systems, especially the thermal management of vehicle lighting systems based on light emitting diodes (LEDs). Lighting systems based on LEDs offer many advantages, including improved energy efficiency and potential for weight reduction. However, such lighting systems also pose a smaller margin of error for thermal management because LEDs can be permanently damaged if their operation temperature exceeds a critical temperature. Furthermore, the output power of LEDs varies significantly with the operation temperature. Therefore, a better thermal management technique is desired for such light systems.

A cooling management system (CMS) based on PCMs appear very attractive for this purpose because a PCM essentially behaves as a thermal switch. When the operation temperature of the lighting systems begins to exceed that of the melting temperature of the PCM, the temperature of the system stops increasing until the PCM is completely melted. Therefore, CMS based on PCMs show good promise to tightly control the temperature of LEDs. But as described above, the operation time of the CMS is fundamentally limited by the melting time of the PCM, which was a key parameter to be investigated in this study. The investigation was focused on maximizing the operation time of the CMS while still operating under specified sizing and other restraints.

More specifically, PCMs are characterized by their T_M, ΔH, and their T_S and T_L (Other properties may need to be considered for specific applications, e.g., ρ, chemical stability, safety, and flammability [44]). Once the operating temperature of the system being cooled reaches the T_L of the PCM, the PCM begins to melt and stores the thermal energy that the system releases during this process. The amount of thermal energy that the PCM can store depends on its ΔH and amount. During the melting process, the PCM and, therefore, the system temperature remain constant. The duration of the melting process delays the system from reaching its maximum operational temperature, which prolongs the operational time of the system where the operational time is defined as the amount of time it takes for the system to reach its maximum operational temperature. This operational time gain depends heavily on the PCM mass ratio and the PCM thermophysical properties k, ρ, ΔH, T_M, and C_P. The configuration of the unit containing the PCM, such as the thermal properties and the distribution of a thermal conductivity enhancer that encapsulates the PCM, also affects the system's performance [45, 46].

It is known that the PCM's conductivity plays a very important role in the cooling system's performance [45]. Higher conductivity is usually preferred, because it aids in heat distribution, more uniform PCM melting process, and overall effectiveness of the CMS. Consequently, a higher conductivity of the PCM would increase the heat transfer rate and prolong the operational time of the lighting system. However, many PCMs have relatively low conductivity. For example, organic PCMs exhibit relatively low thermal conductivity, even though they, in comparison with metallic PCMs, are less corrosive, more readily available, and less costly. In order to improve the overall effective conductivity of the CMS to leverage the advantages of such organic PCMs, many researchers suggest filling the PCM into a honeycomb structure or mixing it with metal foam conductors [46, 47]. However, with a fixed size for the CMS unit, increasing the effective conductivity of the system will decrease the effective mass of the PCM material. This, in turn, reduces the heat storage potential of the system, thereby, reducing the operational time of the lighting system. Hence, this paper analyzed the optimal volume fraction of the PCM for attaining the maximum operational time at a fixed size for the CMS unit.

2.4 Problem Formulation

During the phase change process (melting or solidification), the PCM encapsulated in a porous material, in this case, metal foam (MF), can exist in three states: solid, liquid, and a two phase mixture. Additionally, the thermal properties of a PCM-MF matrix are different from the constituent properties. To simplify the mathematical model, the PCM–MF combination can be treated as a body of uniform equivalent physical and thermal properties—principally C_P, ρ and k of the PCM and MF. The effective properties of the mixture are calculated based on the volume ratio, ε of the PCM material in the mixture, as follows:

$$(C_P)_{eff} = [(1-\varepsilon)(\rho C_P)_{MF} + (\rho C_P)_{PCM}] / \rho_{eff} \tag{2.1}$$

where

$$\rho_{eff} = (1-\varepsilon)\rho_{MF} + \varepsilon\ \rho_{PCM} \tag{2.2}$$

and as derived in [48],

$$k_{eff} = \left(\left(\frac{2}{\sqrt{3}}\right) \left(\begin{array}{l} \dfrac{r\left(b/L_f\right)}{k_f + (1/3)\left(1+b/L_f\right)\left(k_s - k_f\right)} \\ + \dfrac{(1-r)\left(b/L_f\right)}{k_f + (2/3)\left(b/L_f\right)\left(k_s - k_f\right)} \\ + \dfrac{\sqrt{3}/2 - b/L_f}{k_f + \left(4r/3\sqrt{3}\right)\left(b/L_f\right)\left(k_s - k_f\right)} \end{array} \right) \right)^{-1} \tag{2.3}$$

where b/L_f is given by the following expression

$$\frac{b}{L_f} = \frac{-r + \sqrt{r^2 + \dfrac{2}{\sqrt{3}}(1-\varepsilon)\left(2 - r\left(1 + \dfrac{4}{\sqrt{3}}\right)\right)}}{\dfrac{2}{3}\left(2 - r\left(1 + \dfrac{4}{\sqrt{3}}\right)\right)} \tag{2.4}$$

Or, in a more simplified yet reasonably accurate form, k_{eff} can be calculated as follows [49]:

$$k_{eff} = (1-\varepsilon)k_{MF} + \varepsilon\ k_{PCM} \tag{2.5}$$

This analysis performed in the paper was based on Equation (2.5). Also, instead of tracking the liquid-solid front explicitly, the enthalpy-porosity formulation can be used in this type of application. The two phase zone is treated as a porous zone with porosity equal to β, the liquid fraction, which is defined in the following Equation (2.6):

$$\begin{aligned} &\beta = 0 && \text{if } T < T_s \\ &\beta = \frac{T - T_s}{T_l - T_s} && \text{if } T_s < T < T_l \\ &\beta = 1 && \text{if } T > T_l \end{aligned} \tag{2.6}$$

With this definition (also referred to as the lever rule [50]), an enthalpy-porosity technique can be used for modeling the melting process [46]. The two phase zone is a region in which β of the PCM lies between 0 and 1, with 1 corresponding to the PCM being fully melted and 0 corresponding to the PCM being fully solid. The two phase zone is modeled as a “pseudo" porous medium in which the porosity decreases from 1 to 0 as the material melts. When the material has fully melted in the cell, the porosity becomes 0.

The enthalpy of the material is computed as the sum of h_{sens}, and ΔH:

$$H_{tot} = h_{sens} + \Delta H \tag{2.7}$$

where

$$h_{sens} = h_{ref} + \int_{T_{ref}}^{T} c_p dT \tag{2.8}$$

The latent heat content of the PCM (a mixture of melted liquid and unmelted solid), *L*, can now be written in terms of *L* and β as follows:

$$\Delta H = \beta L \tag{2.9}$$

Obviously, the latent heat content, *L*, varies between zero (for a pure solid) and *L* (for a liquid).

For solidification/melting problems, the energy equation can be written as [50]

$$\partial\left(\rho C_P T\right)\big/\partial t = \nabla\cdot\left(k\nabla T\right) + S_h \tag{2.10}$$

where S_h is the source term to account for the latent heat variation during the melting process. It is represented by:

$$S_h = -\rho\,\partial\left(\Delta H\right)\big/\partial t \tag{2.11}$$

And ΔH is calculated utilizing the lever rule from Equation (2.6).

Now, temperature can be solved for by the interaction between the energy equation and the liquid fraction equation.

2.5 The Physical Problem and the PCM Material Properties

The physical problem was defined according to the design constraints of an LED light system. The heat input from the vehicle’s lighting system was given to be a total of 73.5 W. The maximum permissible temperature of the lighting system was not to exceed

90°C and the ambient temperature was given to be 27°C. The problem is assumed to be conduction-dominated within the CMS unit, thus the internal natural convective heat transfer effect of the PCM can be neglected.

The geometry of the CMS consisted of a cylindrical container of aluminum material. The container contains a mixture of a PCM suspended in an aluminum metal foam. Figure 2- 1 shows the sketch of the CMS unit. The diameter (*D*) and height (*H*) of the domain were 10 cm and 10 cm, respectively.

Three operating conditions were considered in this investigation, by assuming three different boundary conditions. In the first case the unit is assumed to be fitted outside the engine-hood, exposed to an ambient temperature of 27°C, and air velocity of 40 kilometers per hour (the average speed of the vehicle). This gave an average convective heat transfer coefficient of 14 W/m^2-K. This case was considered to be the forced convection (FC) condition.

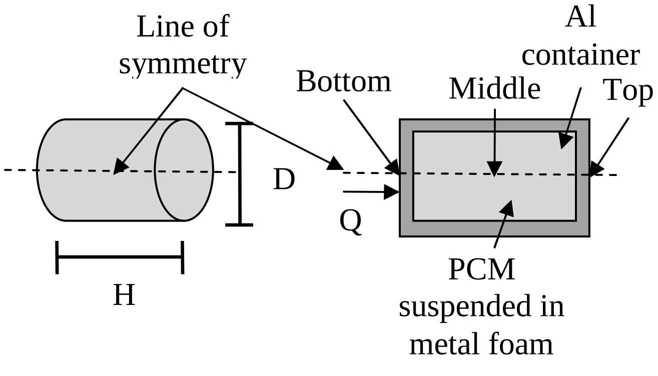

Figure 2- 1. Problem schematic.

In the second case the unit is assumed to be installed outside the engine-hood, but with the vehicle at rest. In this case, the temperature that the unit was exposed to is the ambient temperature of 27°C. Natural convection would be present in this case, therefore, a value of h = 5 W/m^2-K was then determined. This case was considered to be the natural convection (NC) condition.

Material	**ρ [kg/m^3]**	**C_P [J/kg-K]**	**ΔH [J/kg]**	**T_M [^{o}C]**
MF: Al	**2700**	**963**	**-**	**-**
PCM: Climsel C 70	**1700**	**3600**	**280800**	**70**
PCM: Therma-sorb-175	**930**	**2000**	**200000**	**79**
PCM: RT80	**920**	**2400**	**175000**	**81**
PCM: Triacontane	**810**	**2050**	**251000**	**65**

Table 2- 1. Properties of some PCM materials and Al Metal Foam

Finally, the third case assumed the unit was to be installed under the engine-hood. The temperature of the environment under the hood (engine temperature) would be extremely high, much higher than the maximum allowable temperature of the protected lighting system. Thus, the unit must be completely isolated. This is considered to be the worst operating condition possible, since the unit is operating without any external cooling. This case was considered to be the adiabatic (AD) condition.

The thermophysical properties of the PCM and the aluminum metal foam used in this study are listed in Table 2- 1, and are assumed to remain constant over the entire temperature range encountered in the operation.

2.6 Numerical Analysis

The commercially available software programs Fluent and ANSYS were used to perform a control-volume-based technique that converts the governing equations into algebraic equations to be solved. This control-volume technique consisted of integrating the governing equations about each control-volume, yielding discrete equations that conserve each quantity on a control-volume basis [51].

A point implicit (Gauss-Seidel) linear equation solver was used in conjunction with an algebraic multigrid (AMG) method to solve the resultant scalar system of equations for the dependent variable in each cell.

For transient simulations, the governing equations were discretized in both space and time. Temporal discretization involved the integration of every term in the differential equations over a time step Δt.

A fully implicit integration scheme was used for integration of the unsteady term (i.e., using “the future time level”). The advantage of the fully implicit scheme is that it is unconditionally stable with respect to the time step size. A grid-independence study was carried out to test the sensitivity of the solution to the grid size.

2.7 Results and Discussion

It is very important to select a PCM with a T_M that is close to the maximum allowable temperature of the protected system to attain its best performance [52].

According to our survey, the PCMs listed in Table 2- 1 are among the most suitable organic PCMs which satisfy the above condition for the thermal management of the LED lighting system.

Use of a different PCM involves a tradeoff among various factors, e.g., the cooling effectiveness, the operational time, and the thermal protection. For example, as can be seen, ClimSel C70 clearly has the highest ΔH, k, and (ρC_P). However, its T_M is too low when compared with the target protection temperature (90 ^{0}C), which will be overprotective in practice. Thermasorb-175 and RT80 have a much closer T_M to that of the failure temperature of the lighting system. However, these two (along with RT80) have much lower values for ($\rho\, C_P$) and ΔH.

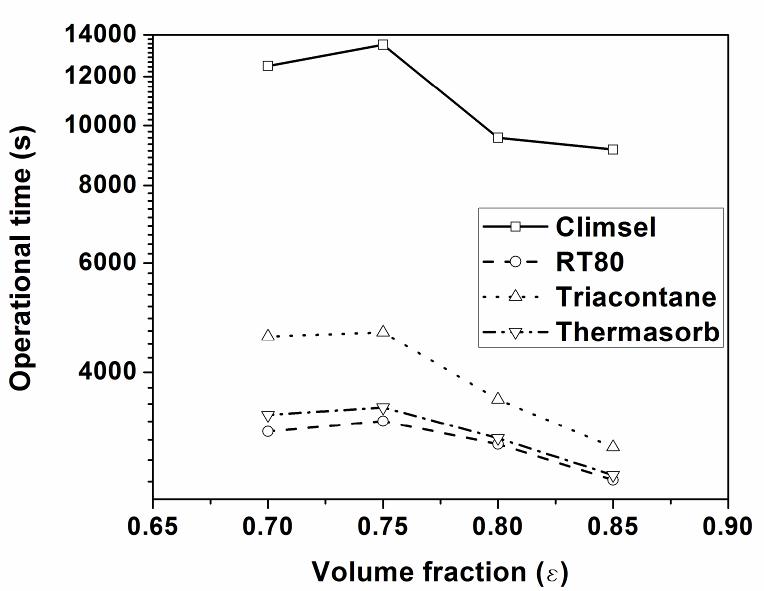

Figure 2- 2. Maximum operational time achieved for various ε's of four different PCM's.

In this study, all four PCMs were tested over a range of volume fractions in order to see which PCM can give the longest operational time for the lighting system. The results of this investigation were plotted in Figure 2- 2. Figure 2- 2 clearly shows that all four PCM-MF mixtures yield about the same duration of operational time at a volume fraction of $\varepsilon = 0.75$.

Figure 2- 2 also indicates that ClimSel C70 yielded the longest operational time in comparison with the rest of PCMs. Therefore, ClimSel C70 was chosen for the rest of the study to be discussed below.

To illustrate the operation of the CMS more closely, we calculated the liquid fraction (β) at different operational times. Time zero was defined as the time when the LEDs were turned on to generate a heat flow (Q) of 73.5 W. Figure 2- 3 shows the variation of β versus the operational time of the PCM-MF mixture at the three types of boundary conditions as mentioned above: the forced convection, FC, the natural convection, NC, and the adiabatic, AD. Figure 2- 3 shows that under all boundary conditions, the PCM was fully melted after a certain duration of operation under the given conditions (heat load, driving velocity, geometry of the CMS, etc.). As expected, the FC boundary conditions corresponded to the longest melting time (~ 12,000 seconds in this case), which defines the operational time of the CMS. Under the AD boundary condition, heat transfer out of the system is zero. Thus, the time needed to melt the PCM was the shortest. It is desirable to prolong the operational time, and one possible strategy involves using a different geometry of the CMS.

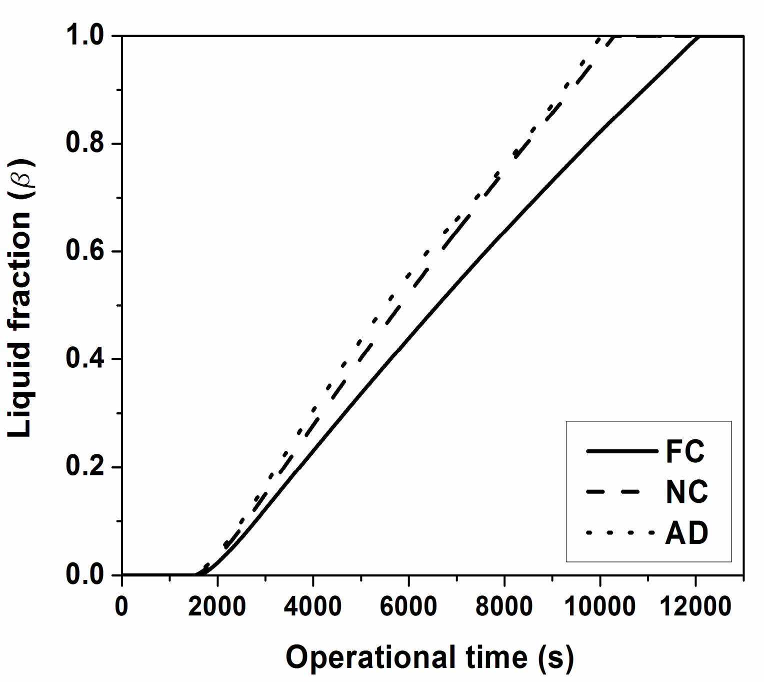

Figure 2- 3. The time evolution of β of the PCM.

Figure 2- 4, Figure 2- 5, and Figure 2- 6 show the transient temperature history of the CMS at different locations under the three boundary conditions, the FC, NC and AD cases, respectively. These figures illustrate the rise of the temperature as a function of operating time at the bottom, the middle, and the top sections of the CMS. As expected, the bottom section of the unit will reach T_M and the failure temperature first, because it is in direct contact with the heat source (i.e., the LED array). Therefore, the temperature at the bottom section essentially defines the operational time of the CMS.

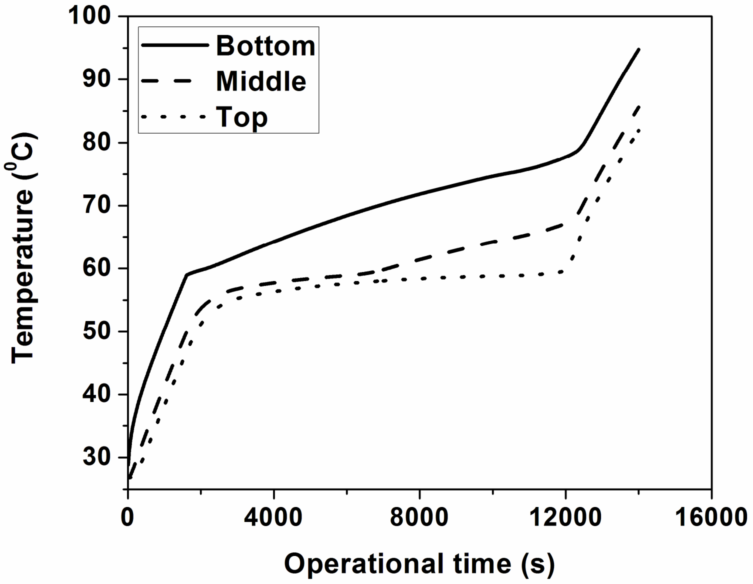

Figure 2- 4. Temperature at different locations within the CMS under the FC boundary condition.

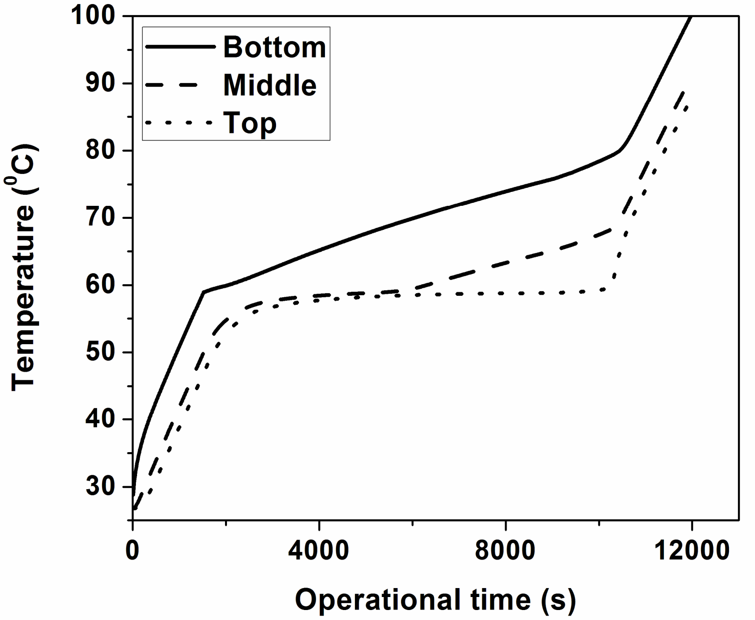

Figure 2- 5. Temperature at different locations within the CMS under the NC boundary condition.

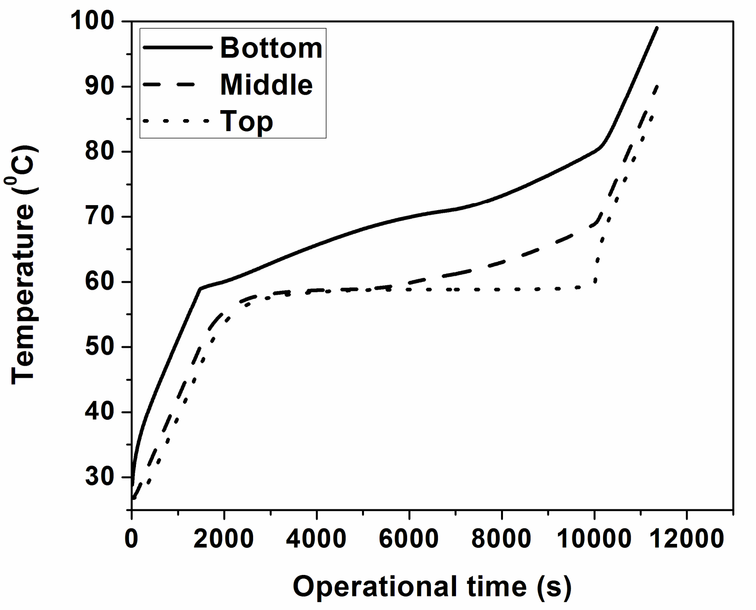

Figure 2- 6. Temperature at different locations within the CMS under the AD boundary condition.

Figure 2- 7 summarizes the time at which the critical temperature was reached under different boundary conditions at different locations. As can be seen, under the FC condition, the most favorable cooling condition, the bottom section reached the critical temperature after 13,490 seconds (3.7 hours) of operation; under the NC condition, the bottom section reached the critical temperature after 11240 seconds (3.1 hours) of operation; and finally, under the AD boundary condition, after 10790 seconds (2.99 hours) of operation.

Again, one possible approach to prolong the operational time of the CMS involves varying the geometry of the CMS. Enlarging the size of the CMS represents a simple, yet effective method. For example, our calculations showed that with a unit size of 20 cm diameter and 20 cm height, an operational time of 18 hours can be obtained under the FC boundary condition. Research is underway to optimize the operational time under various geometrical constraints.

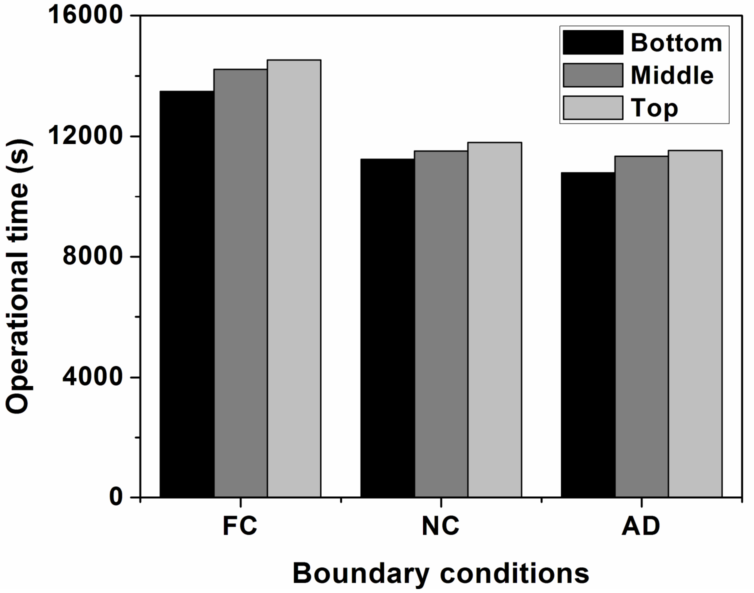

Figure 2- 7. The operational times for all three boundary conditions at three different locations within the CMS.

Lastly, we compared the distinct cooling characteristics between the PCM-based method and the method based on a solid metal sink system (SMS). Figure 2- 8 compares the history of temperature rise at the bottom section using the PCM-based method (the CMS case) and the cooling method based on a solid unit of aluminum (the SMS case). In this comparison, both the CMS and the SMS cases were assumed to have the same geometry as defined in Figure 2- 1; and both cases were assumed to operate under the same conditions as defined previously. As Figure 2- 8 shows, with the SMS system, temperature increased monotonically until it reached an asymptotic value (corresponding to the steady state value). In contrast, with the CMS system, temperature first increased to the melting temperature of the PCM, then remained almost constant around the melting temperature, and finally started increasing again after the PCM was completely melted. This difference clearly elucidates the functionality of the PCM system as a thermal switch to tightly control the temperature.

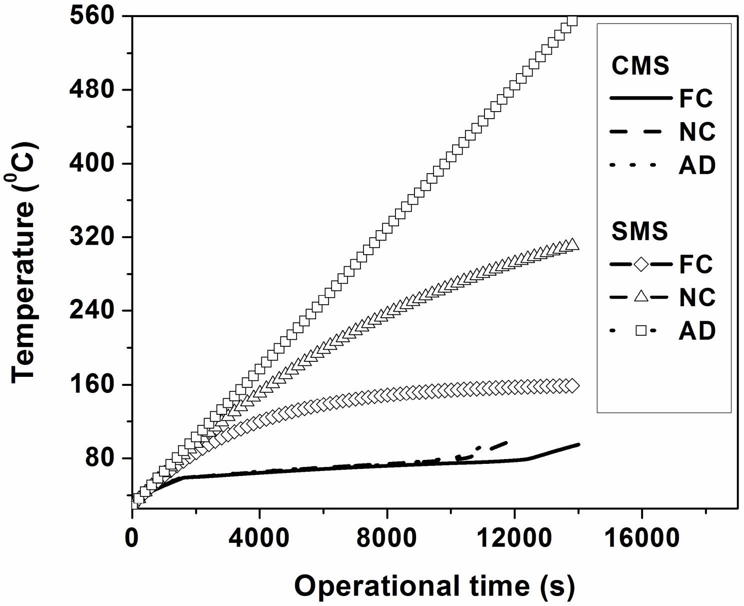

Figure 2- 8. Operational time comparison between SMS and CMS at all three boundary conditions.

2.8 Conclusions and Discussion

The use of PCMs was investigated for the thermal management of LED lighting systems. The advantages of the PCMs to tightly control temperature below the failure temperature of the LEDs were clearly illustrated. The performance and limitations of the PCM-based cooling methods for such applications were examined using extensive numerical simulations. The use of metal foam significantly improved the cooling performance, and the optimal MF fraction was determined. The cooling performance was also compared to a solid metal sink system and was found to offer several distinct cooling characteristics.

Two conclusions can be drawn from this study. First, a well-chosen PCM provides better control of temperature when compared with a metallic heat sink. Second, the operational time of the PCM-based method depends sensitively on several factors, especially the size and geometry of the cooling unit. Research is underway to optimize the design of PCM-based cooling systems under geometrical constraints.

Current ongoing research involves investigating the performance of the PCM-based cooling systems under more realistic boundary conditions, and validating the numerical analysis via experimental tests. In reality, the boundary conditions are characterized by mixed modes of heat transfer, and transient temperatures. Though the rigorous is undergoing, many insights can be obtained from the results presented here. For example, the case with an adiabatic boundary condition represents the worst scenario under a constant under-hood temperature. When the temperature fluctuates (as long as it does not exceed the temperature studied here), the operational time will be prolonged. A prolonged operational time can also be expected when mixed modes of heat transfer are considered.

Chapter 3: Development of a Sensor for Simultaneous Droplet Size and Vapor Measurement Based on Wavelength-Multiplexed Laser Extinction

3.1 Abstract

Multiphase flows involving liquid droplets in association with a gas flow occur in many industrial and scientific applications. Recent work has demonstrated the feasibility of using optical techniques based on laser extinction to simultaneously measure vapor (e.g., vapor concentration and temperature) and droplet properties (e.g., droplet size and loading). This work introduces the theoretical background for the optimal design of such laser extinction techniques, which is termed the WMLE (wavelength-multiplexed laser extinction) technique in this paper. After a brief survey of past work, this paper focuses on the development of WMLE and presents a systematic methodology to guide the selection of suitable wavelengths and therefore optimize the performance of WMLE for a

specific application. WMLE schemes utilizing wavelengths ranging from 0.5 to 10 μm are illustrated for droplet size and vapor concentration measurements through an example of water spray and are found to enable unique and sensitive Sauter mean diameter measurement in the range of ~1 to 15 μm along with accurate vapor detection. A vapor detection strategy based on differential absorption is developed to extend accurate vapor measurement to a significantly wider range of droplet loading and vapor concentration compared with strategies based on direct fixed-wavelength absorption. Expected performance of the sensor is modeled for an evaporating spray. This work is expected to lay the groundwork for implementing optical sensors based on WMLE in a variety of research and industrial applications involving multi-phase flows.

3.2 Introduction

In many scientific and industrial applications, multiphase problems exist in the form of liquid droplets in association with a gas flow. The study of vaporization or condensation of liquid droplets inside a spray is one typical example. In such applications, it would be desirable to monitor both the vapor and the droplets simultaneously.

Numerous laser-based techniques have been developed for the separate characterization of either vapor or droplets. These vapor sensing techniques include laser Rayleigh scattering [53], spontaneous Raman spectroscopy [53], laser-induced fluorescence (LIF) [53, 54], spectrally-resolved absorption [55], and others. Droplet measurement techniques include the measurement of Fraunhofer diffraction of laser radiation by droplets [56], laser phase Doppler anemometry [57], laser extinction [58, 59], and wavelength-multiplexed laser extinction [60]. Each technique has its own advantages and disadvantages and is useful for a certain domain of applications.

However, these techniques are generally not transferable to the simultaneous monitoring of both vapor and droplet properties. Some vapor sensing techniques based on elastic scattering such as the Rayleigh scattering technique or LIF can be extended to measure both vapor and droplets. However, usually the scattering from droplets greatly exceeds that from the vapor, therefore, jeopardizing or even prohibiting an accurate vapor measurement. Similar reasoning precludes the direct combination of one vapor and one droplet measurement technique discussed above for simultaneous vapor and droplet measurements. Furthermore, different techniques usually have different temporal and spatial resolution, and some of the techniques may require wide optical access, so that practical implementation becomes difficult.

Despite these challenges, a few laser-based diagnostic techniques have been attempted for simultaneous characterization of vapor and droplets. Laser Induced Exciplex Fluorescence (LIEF) developed by Melton [61] allowed two-dimensional imaging of vapor and droplets simultaneously under limited conditions. Besides implementation difficulties, however, the LIEF signal is difficult to quantify, and quenching from oxygen limits most of the LIEF applications to nitrogen environments [53]. For more quantitative and realistic applications, Chraplyvy and Tishkoff [62, 63] proposed and applied a method based on a two-wavelength laser extinction strategy to measure vapor concentration and droplet volume fraction simultaneously in an evaporating fuel spray. This technique requires an independent droplet size distribution (or droplet size in the case of mono-dispersed droplets) measurement, and the dynamic range of measurements offered by this technique was limited.

Of the methods investigated thus far, techniques based on laser extinction are especially attractive owing to their relative simplicity in implementation and data interpretation, capability to provide continuous measurement with fast time response, very limited requirement of optical access, and species specificity if wavelengths are well chosen. This paper describes the development of a sensor for simultaneous droplet and vapor measurement based on wavelength-multiplexed laser extinction (WMLE). The first unique feature of this sensor involves the incorporation of laser sources at an arbitrary number of wavelengths to expand sensing capability of the diagnostic to more quantities besides vapor concentration and droplet volume fraction. The second unique feature involves a vapor sensing technique modified from spectrally-resolved absorption, namely differential absorption, to significantly improve the detection limit of vapor sensing. Experimental demonstration and application of the sensor have been reported elsewhere [64, 65]. Here we describe the sensing strategy and analyze the sensor performance. Systematic methodologies are developed to guide the selection of wavelengths to achieve optimized performance for both vapor and droplets measurement, and expected performance is modeled for an evaporating spray.

3.3 Theory

When a collimated light beam at wavelength λ is incident upon a mixture of vapor and droplets, the transmitted beam intensity (I_t) is related to the incident beam intensity (I_0) by

$$\begin{aligned} T(\lambda) &= I_t / I_0 \\ &= \exp[-\tau_{vapor}(\lambda)] \cdot \exp[-\tau_{drops}(\lambda)] \\ &= \exp[-\alpha(\lambda) \cdot X \cdot P \cdot L] \cdot \exp[-\tau_{drops}(\lambda)] \end{aligned} \tag{3.1}$$

where:

$T(\lambda)$ = the optical transmittance at wavelength λ

$\tau_{vapor}(\lambda)$ = the vapor absorbance

$\tau_{drops}(\lambda)$ = the droplet extinction

$\alpha(\lambda)$ = the absorption coefficient of vapor ($\text{cm}^{-1}\cdot\text{atm}^{-1}$)

X = the vapor mole fraction

P = the total (mixture) pressure along the pathlength (atm)

L = the pathlength (cm)

From light scattering theory [66], extinction by a collection of monodisperse spherical droplets is related to the number density and size of the droplets in the following equation

$$\tau_{drops} = C_n \cdot \frac{\pi D^2}{4} \cdot Q(\pi D / \lambda, m) \cdot L \tag{3.2}$$

where:

C_n = the number density of the droplets (cm^{-3})

D = diameter of the droplets (cm)

$Q(\pi D/\lambda,m)$ = the extinction coefficient of a droplet with diameter D at wavelength λ

m = the complex refractive index of the droplets at wavelength λ

$Q(\pi D/\lambda,m)$ is a complex function of the incident wavelength and droplet diameter and calculation of $Q(\pi D/\lambda,m)$ requires numerical methods, except in some special cases. This work uses a Mie scattering algorithm described in [67] to compute the droplet extinction coefficients. In the case of a collection of poly-dispersed droplets, Equation (3.2) needs to be modified as

$$\tau_{drops} = \frac{\pi}{4} C_n L \int_0^{\infty} Q(\pi D/\lambda, m) f(D) D^2 dD \tag{3.3}$$

where $f(D)$ is the droplet size distribution function defined such that $\int_0^{\infty} f(D)dD = 1$, and $f(D)dD$ represents the probability that a droplet has diameter between D and $D+dD$. Due to the lack of fundamental mechanism or model to build droplet size distribution functions theoretically, various distribution functions have been used based on probability analysis or empirical observations. A log-normal function, defined as following, is one of the most commonly used distribution functions:

$$f(D) = \frac{1}{\sqrt{2\pi} D \ln\sigma} \exp[-\frac{1}{2(\ln\sigma)^2} \cdot (\ln D - \ln D_{CM})^2] \tag{3.4}$$

In this equation, σ represents the standard deviation of the distribution (distribution width); and D_{CM} the count median diameter, which means 50% of the droplets in the distribution have diameter smaller than D_{CM} and 50% larger than D_{CM}.

In many calculations and applications, it is convenient to restrict the work to averaged parameters instead of using the complete size distribution function. Based on *f(D)*, many statistical parameters about the droplet distribution can be defined. Two useful parameters, the mean scattering coefficient $(\overline{Q})$ and the Sauter Mean Diameter (D_{32}), are defined as following

$$\overline{Q} = \frac{\int_0^\infty Q(\pi D/\lambda, m) f(D) D^2 dD}{\int_0^\infty f(D) D^2 dD} \tag{3.5}$$

$$D_{32} = \frac{\int_0^\infty f(D) D^3 dD}{\int_0^\infty f(D) D^2 dD} \tag{3.6}$$

Obviously, for a given droplet distribution, $\bar{Q}$ depends on the incident wavelength and some characteristic diameter of the droplets. D_{32} is used as such a characteristic diameter in this paper and this dependence is denoted as $\bar{Q}(\pi D/\lambda, D_{32})$. Figure 3- 1 provides some example calculations to show the variations of Q (for mono-dispersed droplets) and $\bar{Q}$ (for poly-dispersed droplets) with droplet size at three wavelengths for water droplets. In the case of poly-dispersed droplets, size distribution functions are taken to be the log-normal function defined in Equation (3.4) with different distribution widths, as illustrated in the insert of Figure 3- 1. Refractive indices used in the calculations shown in Figure 3- 1 are from measurements made in [68, 69]. An important observation is that the positions of principal maxima of the extinction coefficient curve display only a weak dependence on the width (σ) of the log-normal distribution functions. Furthermore, a weak dependence on the distribution functions is found both in our work and in studies elsewhere [58], especially when the distribution width (characterized by the standard deviation of the distribution function) is large. Also, note the insensitivity of extinction coefficients to distribution width at a wavelength of 10 μm.

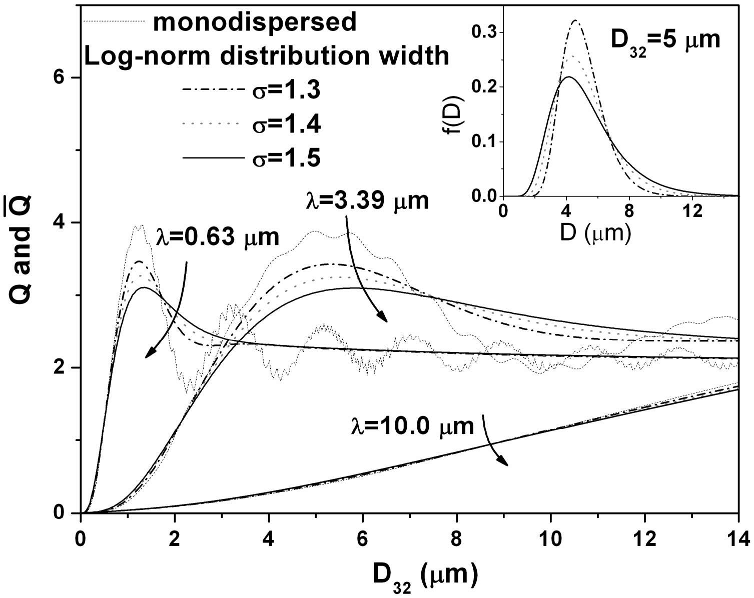

Figure 3- 1. Extinction coefficients at three wavelengths for water droplets at a temperature of 22^{0}C with various size distribution functions, as shown in the inset. Refractive indices are taken to be m=1.335 at λ=0.6328 μm, m=1.42-0.0195*i* at λ=3.39 μm, and m=1.218-0.0508*i* at λ=10 μm.

Finally, by introducing a new parameter, the droplet volume fraction C_V, Equation (3.2) and (3.3) can be transformed into the following forms

$$\tau_{drop} = \frac{3C_V Q(\pi D/\lambda, m)L}{2D} \text{ for mono-dispersed droplets} \qquad (3.7)$$

and

$$\tau_{drop} = \frac{3C_V \bar{Q}(\pi D_{32}/\lambda, m)L}{2D_{32}} \text{ for poly-dispersed droplets} \qquad (3.8)$$

where C_V is defined as the volume fraction occupied by liquid droplets along the pathlength, and can be calculated by the following equations

$$C_V = C_n \cdot \frac{\pi}{6} D^3 \quad \text{for mono-dispersed droplets} \qquad (3.9)$$

and

$$C_V = C_n \int_0^\infty \frac{\pi}{6} D^3 f(D) dD \text{ for poly-dispersed droplets} \qquad (3.10)$$

3.4 Droplet Measurement

3.4.1 Concept

At wavelengths where vapor does not absorb (i.e. $\alpha(\lambda) = 0$), the optical transmittance is only due to droplet extinction and is given by

$$T(\lambda) = \exp[-\tau_{drops}(\lambda)] \qquad (3.11)$$

where $\tau_{drops}(\lambda)$ is given by Equation (3.7) or (3.8).

Transmittance measurement at one wavelength is not sufficient to extract droplet information because of the multiple unknowns (C_n and D) in Equation (3.11). If transmittance measurements are performed at multiple wavelengths (e.g. λ_1 and λ_2), then from Equation (3.7) and (3.8) we obtain

$$\frac{\tau_{drops}(\lambda_1)}{\tau_{drops}(\lambda_2)} = \frac{Q(\pi D / \lambda_1, m)}{Q(\pi D / \lambda_2, m)} = R \quad \text{for mono-dispersed droplets} \qquad (3.12)^*$$

and

$$\frac{\tau_{drops}(\lambda_1)}{\tau_{drops}(\lambda_2)} = \frac{\bar{Q}(\pi D_{32} / \lambda_1, m)}{\bar{Q}(\pi D_{32} / \lambda_2, m)} = R \quad \text{for poly-dispersed droplets} \qquad (3.13)^*$$

Equations (3.12) and (3.13) state that the ratio of measured extinction at wavelength λ_1 and λ_2 only depends on droplet size (or size distribution function) and equals the ratio of extinction coefficients (R) at these wavelengths. Theoretically, by measuring the ratio of extinction at multiple wavelengths and solving Equation (3.12) or (3.13), the droplet size or size distribution function can be inferred. Figure 3- 2 provides an example calculation of the ratio of extinction coefficients (R) at two wavelengths (λ_1=1.5 and λ_2=0.5 μm for water droplets to illustrate this concept. For instance, if the ratio of extinction at λ_1=1.5 and λ_2=0.5 μm is measured to be 0.8, then solving Equation (3.13) will yield D_{32} ~ 1.6 μm for the given droplets, as shown graphically in Figure 3- 2.

---

[*] Due to symmetry, $\lambda_1 > \lambda_2$ is assumed for the discussions of droplet size measurement in this work.

After droplet size or distribution function is determined, other quantities of the spray, such as the droplet number density (C_n) and droplet volume fraction (C_V), can be determined by the absolute value of the laser extinction measured at either wavelength.

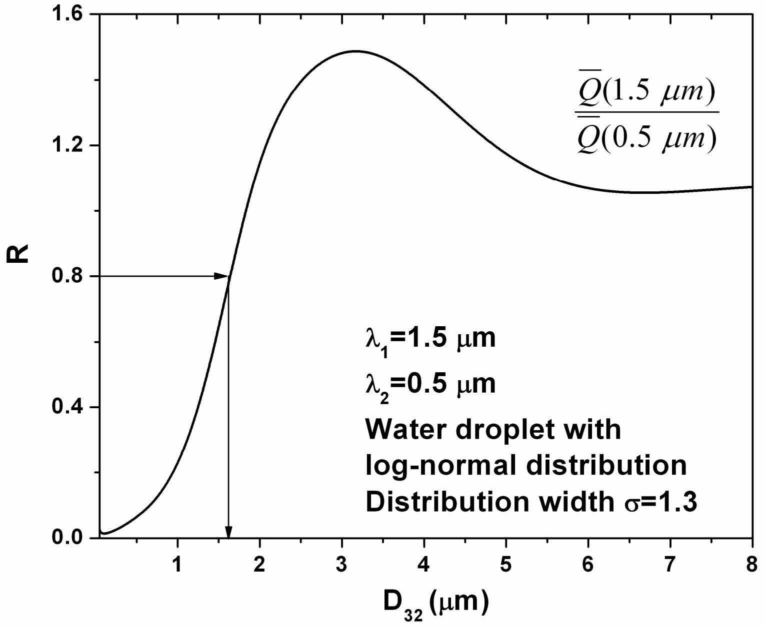

Figure 3- 2. Ratio of extinction coefficients between two wavelengths, λ_1=1.5 and λ_2=0.5 μm for water droplets at 22^{0}C with a log-normal size distribution function.

Variations of this technique have been previously developed and employed using two [59, 70, 71] or three wavelengths [72] ranging from 0.3 to 3.4 μm. These studies achieved droplet size measurement ranges within $0.2<D_{32}<4$ μm. The continuing development of laser sources and related wavelength-multiplexing technologies in recent years renders it feasible to extend this scheme to include a larger number of multiplexed laser sources spanning a wider range of wavelengths. Consequently we contemplate the potential advantages of this extension, for example, to achieve more sensitive droplet size determinations over a wider range.

3.4.2 Selection of Wavelengths

Obviously, it is most desirable to measure the size distribution function for a complete description of the collection of droplets. However, it would be also advantageous to develop a method to guide the selection of wavelengths for optimized droplet size measurement based on a mean diameter of the droplets, rather than the size distribution function. Moreover, under some cases, droplet size can be measured with reasonable accuracy without detailed knowledge about the distribution function [59]. Therefore, this section discusses the selection of wavelengths based on D_{32} to achieve optimized droplet size measurement for a known distribution function.

Three quantitative criteria to define "*optimized droplet size measurement*" at selected wavelengths are first developed from the observations made in Figure 3- 2:

Criterion A. For each combination of two wavelengths, the ratio of extinction coefficients (R) is monotonic only over a certain range of droplet diameter (D_{32}) and the lower limit of this range is denoted by $D_{\min}^{A}$ and upper limit $D_{\max}^{A}$ as shown in Figure 3- 3. The lower limit ($D_{\min}^{A}$) is zero and upper limit ($D_{\max}^{A}$) about 3.2 μm for the combination of λ_1=1.5 and λ_2=0.5 μm for the water droplets specified in Figure 3- 2. For a D_{32} outside this range, this combination of two wavelengths becomes insufficient to provide a unique determination of D_{32}. Criterion A requires that the selected wavelengths provide unique determination of droplet size over the range of droplet size to be measured.

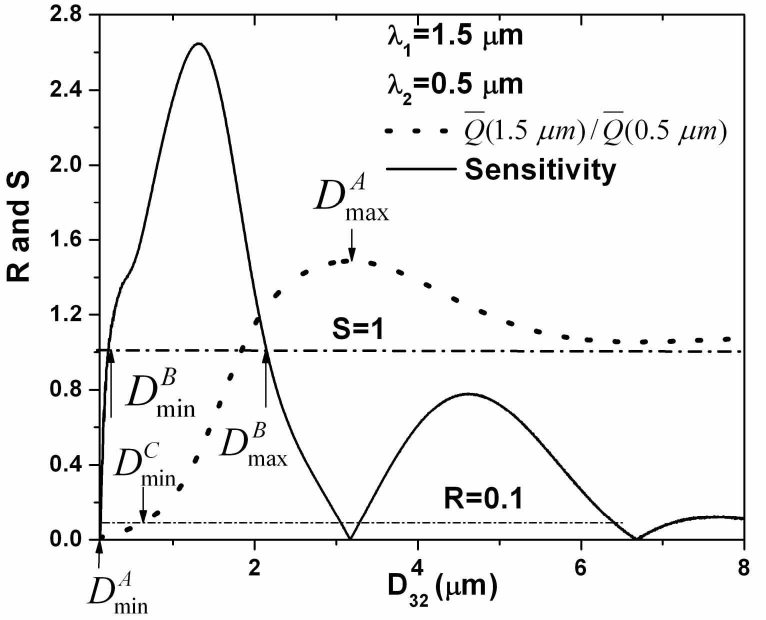

Figure 3- 3. Ratio of extinction coefficients between two wavelengths, λ_1=1.5 and λ_2=0.5 μm, for water droplets with a log-normal size distribution function. And the sensitivity of this ratio for D_{32} measurement.

Criterion B. For each combination of two wavelengths, the ratio of extinction coefficients (R) is only sensitive to droplet diameter (D_{32}) over a certain range of D_{32}. As for the calculation shown in Figure 3- 2, R remains virtually unchanged for the range of D_{32} near $D^A_{\max}$ and/or greater than 6 μm. Obviously, insensitivity of R to D_{32} is not desirable for droplet size measurement. Criterion B requires that the selected wavelengths provide sensitive determination of droplet size over the range of droplet sizes to be measured.

In this work, sensitivity of droplet sizing (S) is quantified by the following equation:

$$S = \left| \frac{dR/R}{dD_{32}/D_{32}} \right| \tag{3.14}$$

A large S implies that a small proportional change in D_{32} results in large proportional change in R; therefore, sensitive determination of D_{32} is enabled. The sensitivity for the wavelength combination described in Figure 3- 2 is calculated in Figure 3- 3. Different applications may require different levels of sensitivity. Here we define a minimum sensitivity of unity (S=1) for the purpose of this discussion. Consequently, a combination of two wavelengths is considered unacceptable over the range of D_{32}, where S of this combination is less than unity, and the upper limit of this range is denoted by $D_{\max}^{B}$ as shown in Fig. 3. Calculations in Figure 3- 3 show a $D_{\max}^{B}$ of about 2.2 μm for the wavelength combination used in Figure 3- 2.

Criterion C. For each combination of two wavelengths, the ratio of extinction coefficients (R) is very small over a certain range of D_{32}. Based on Equation (3.12) or (3.13), very small R implies either very strong or very weak extinction at one of the wavelengths. However, both very strong extinction and very weak extinction impair signal to noise ratio (SNR) of the measurement. A transmittance (I_t/I_0) between 0.4 and 0.9 is recommended for optimum extinction measurement [73]. Based on this recommendation and Equation (3.1), the optimum R for droplet sizing should lie between 0.1 and 10. Criterion C requires that the ratio of extinction coefficients at the selected wavelengths be between 0.1 to 10 to ensure optimum SNR over the range of droplet size to be measured. This criterion usually imposes a lower limit on the applicable range of a combination of two wavelengths (under the assumption that $\lambda_1 > \lambda_2$ in Equation (3.12) and (3.13)) and this limit is denoted by $D_{\min}^{C}$ as shown in Figure 3- 3.

More detailed discussion of these criteria can be found in [60]. Based on these three criteria, a method is developed to select the minimum number of wavelengths for droplet size distribution measurement. As an example application of these criteria and the wavelength selection method, here we describe the design of sensor to measurement the D_{32} of water aerosols following the lognormal distribution as defined in Equation (3.4) using wavelengths in the range from 0.25 to 10 μm. Forty wavelengths uniformly spaced between 0.25 and 10 μm (the spacing is 0.25 μm) are considered. The Mie extinction coefficient at each wavelength is calculated using the refractive index of water at 22^0C provided in [68, 69]. Then, the mean extinction coefficients are calculated for a given distribution, specified by a distribution width, σ, and a counter median diameter, *DCM* (or equivalently a Sauter Mean Diameter, D_{32}). All the possible ratios formed from these mean extinction coefficients are then examined against the three criteria described above to select the optimized wavelengths. Five wavelengths, 0.25, 0.5, 1.5, 4.0 and 10 μm, are selected for $0.7 < D_{32} < 12$ μm and $1.2 < \sigma < 1.6$, where a σ of 1.2 corresponds to a very narrow distribution and a σ of 1.6 to a dispersed distribution spanning more than one decade. Therefore, a WMLE scheme composed of these wavelengths will enable sensitive and unique determination of the mean droplet size over a wide range of distributions.

3.4.3 General WMLE for Droplet Measurement

Although the analysis in the preceding section is based on water droplets with a specific size distribution function, extension of the major conclusions obtained from this analysis to other droplet systems is straightforward.

First. we consider the extension to droplets with other distribution functions. The conclusions obtained regarding each criterion are not sensitive to size distribution functions, because the analysis depends primarily on the locations of principal maxima of the extinction coefficient curves, which are relatively insensitive to droplet size distribution functions as discussed in Figure 3- 1.

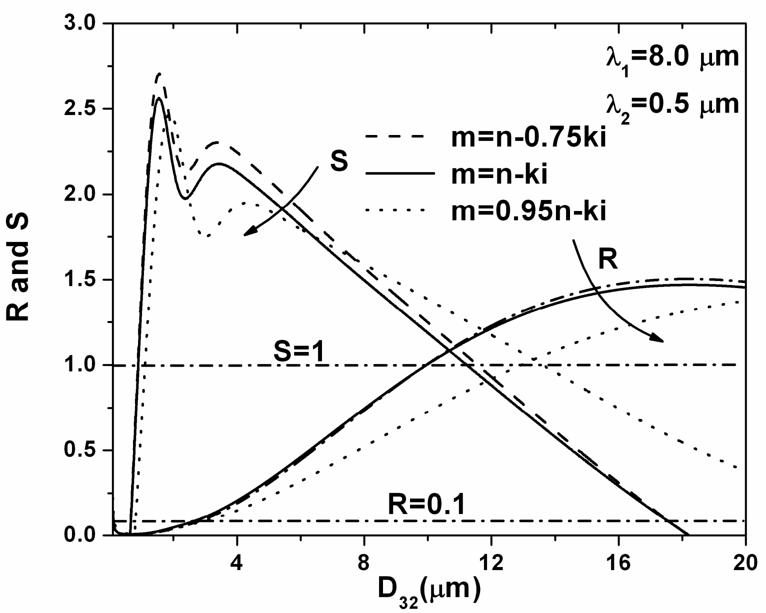

Figure 3- 4. Ratio of extinction coefficients between two wavelengths (λ_1=8.0 and λ_2=0.5 μm) and the sensitivity of this ratio for D_{32} measurement with a log-normal size distribution function. Imaginary and real part of the refractive index at these wavelengths are assumed to change separately in the calculation.

Second we consider the extension to other droplets than water, for example hydrocarbon fuel droplets or even composite fuel droplets. This consideration is essentially the consideration of the dependence of the above conclusions on the refractive indices of the droplets at the selected wavelengths. Our calculations show that the locations of principal maxima of the extinction coefficient curves have a weak dependence on the imaginary part of the refractive index but a strong dependence on the real part of the refractive index. At wavelengths where the imaginary part of the refractive index is not very large, the effect of imaginary part is negligible. Figure 3- 4 presents some example calculations to illustrate this analysis. In Figure 3- 4, the ratio of mean extinction coefficient between 0.5 and 8 μm are calculated assuming different imaginary and real parts of the refractive index. Figure 3- 4 shows that a 25% decrease in the imaginary part of the refractive index has negligible impact on R and S and, consequently has negligible impact on the applicable range of this wavelength combination for droplet size measurement. However, a small increase in the real part of the refractive index causes obvious shifts of the principal maxima of the extinction coefficients toward smaller D_{32}, and, consequently, the ratios of the extinction coefficients will behave monotonically over a narrower D_{32} range, and vice versa. Figure 3- 4 illustrates this strong dependence by showing that a 5% decrease in the real part of the refractive index results in substantial change in R and S. In this case, the real part of the refractive index is decreased. Therefore, the range in which R behaves monotonically is widened as expected. On the contrary, adoption of the scheme designed for water droplets at the end of section 3.2 to droplets with a real part of the refractive index larger than that for water droplets (e.g., heptane or decane droplets) will result in a narrower applicable range of D_{32}. More wavelengths can be added to maintain the same D_{32} measurement range.

Finally, we consider the extension to droplets with different temperatures. The influence of temperature on wavelength selection derives from the variation of refractive index with temperature of the droplets. Therefore, a similar analysis made in the above paragraph applies here except that an increase in droplet temperature usually causes a decrease in the real part of the refractive index. Therefore, adoption of the scheme designed for water droplets at a temperature of 22^0C at the end of section 3.2 will yield a wider applicable range of D_{32} at a higher temperature, as illustrated by the calculations shown in Figure 3- 4 with decreased real part of the refractive index.

In summary, this section has described a strategy based on WMLE for droplet size measurement and investigated the optimum wavelength selection in a spectral range from 0.25 to 10 μm. An arbitrary number of wavelengths over wider spectral range can be incorporated into the WMLE scheme to achieve simultaneous measurement of multiple quantities in wider droplet size ranges.

The current availability of laser sources in a wide spectral range from deep UV (~ 100 nm) to far IR (~1 mm) facilitates consideration of a general WMLE concept. For example, a large group of gas lasers operate across the wavelength range from about 100 nm to 1 mm. One of the most commonly used devices in this group, the He-Ne laser, generates wavelengths such as 0.5435, 0.6328, 1.152, and 3.391 μm. Another gas laser based on the CO_2 molecule lases between a wavelength range from 9.2 to 11.4 μm and from 4.6 to 5.8 μm when frequency-doubled. Therefore, the He-Ne and CO_2 lasers can provide the wavelengths shown in Figure 3- 1. Another group of lasers, the semiconductor lasers, provide wavelengths ranging from about 600 nm to 30 μm; especially in the spectrum from 0.6 to 1.7 μm, the semiconductor lasers can generate virtually any wavelength. Hence the 0.63 μm wavelength used in Figure 3- 1 can alternatively be provided by a semiconductor laser. Being wavelength tunable, many of the semiconductor lasers can be employed to provide the desired wavelength and avoid interference vapor absorption. Besides the gas and semiconductor lasers, other common laser devices commercially available include solid-state and dye lasers whose output wavelengths range from about 200 nm to 3.9 mm and about 300 to 750 nm respectively. These laser devices provide a great many wavelengths in a wide spectral range and will significantly enhance the development of the WMLE technique.

3.5 Vapor Concentration Measurement

3.5.1 Concept

Theoretically, after the contribution from droplet extinction is known from the droplet measurement, the vapor concentration could be obtained from the measurement of extinction at a wavelength where vapor absorbs [62, 63, 74]. However, the accuracy of this method is jeopardized when the contribution from droplet extinction is larger than that from vapor absorption (i.e., $\tau_{drops} > \tau_{vapor}$) even when τ_{vapor} itself is large enough to allow accurate vapor measurement, therefore limiting the applicable range of this method. An alternative strategy has been sought to extend the vapor detection range.

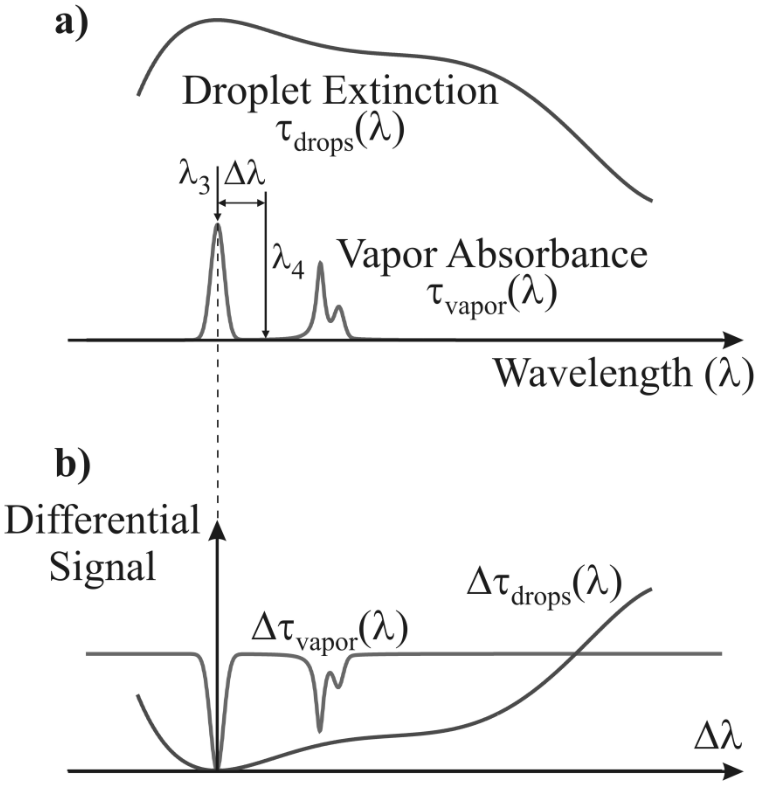

Figure 3- 5. Schematic of differential absorption strategy for vapor measurement.

Our approach for vapor sensing is based on a differential absorption concept. This concept takes advantage of the observation that vapor absorption varies much more rapidly with wavelength than the droplet extinction, based on the fact that vapor spectra is spectrally narrower than corresponding liquid spectra. Figure 3- 5 illustrates this concept schematically, with λ_3 as the vapor detection wavelength. When extinction from droplets exceeds that from vapor absorption as shown in part a) of Figure 3- 5 (i.e. $\tau_{drops}(\lambda_3) > \tau_{vapor}(\lambda_3)$), vapor measurements at this wavelength suffer by interference from strong droplet extinction. However, as shown in part b) of Figure 3- 5, the differential vapor absorption between λ_3 and another wavelength λ_4 (defined as $\Delta\tau_{vapor} = |\tau_{vapor}(\lambda_3) - \tau_{vapor}(\lambda_4)|$), can be comparable or larger than the differential droplet extinction (defined as $\Delta\tau_{drops} = |\tau_{drops}(\lambda_3) - \tau_{drops}(\lambda_4)|$), therefore extending accurate vapor detection into a wider dynamic range.

3.5.2 Selection of Wavelengths

Obviously the selection of wavelengths (λ_3 and λ_4) to optimize vapor detection depends on the spectra of the specific vapor and liquid under consideration. This section again uses water as an example to illustrate a methodology for wavelength selection, but the approach is also applicable to other vapor and liquid systems.

We first examine the dependence of differential droplet extinction ($\Delta\tau_{drops}$) on selected wavelengths (λ_3 and λ_4) with the goal of minimizing differential droplet extinction. Substitution of Equation (3.7) (from mono-dispersed droplets) into the definition of $\Delta\tau_{drops}$ yields

$$\Delta\tau_{drops} = \frac{3C_V\,|Q(\lambda_3, D) - Q(\lambda_4, D)|\,L}{2D} = \frac{3C_V L}{2D}\cdot\Delta Q \qquad (3.15)$$

Therefore the dependence of $\Delta\tau_{drops}$ on selected wavelengths is equivalent to the dependence of ΔQ (i.e. the differential extinction coefficient) on selected wavelengths.

Figure 3- 6 shows the droplet extinction coefficient and vapor absorption over wavelength in a spectral range from 0.5 to 9 μm for water vapor and droplets with two

diameters, using the liquid spectra data of water measured in [68, 69]; and the vapor spectra is simulated using HITRAN 2004. Note the relative slow variation of extinction coefficient compared to that of vapor with wavelength, as mentioned before. Examination of ΔQ at different combinations of λ_3 and λ_4 within this spectral range shows a general profile of ΔQ similar to that shown in Figure 3- 7, where λ_3 is chosen to be 5 μm.

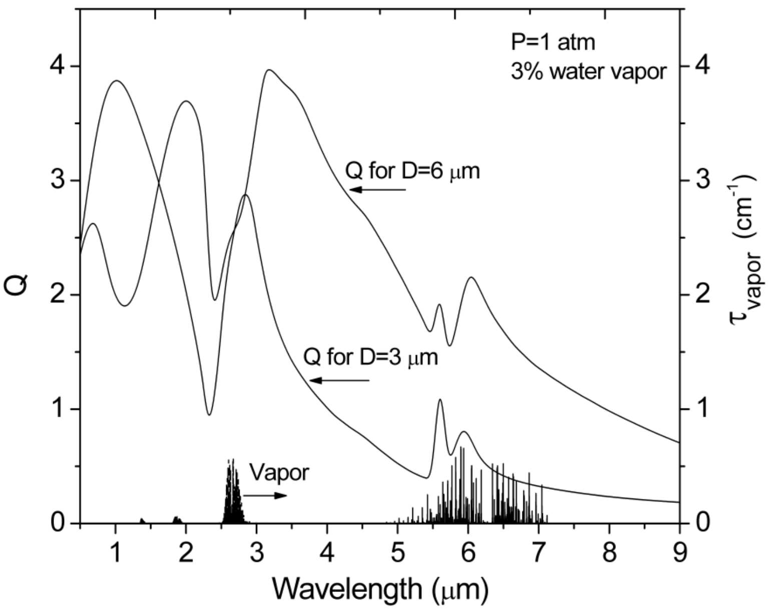

Figure 3- 6. Extinction coefficients for water droplets with different diameters and vapor absorbance from water vapor from 0.5 to 9 μm at 22^{0}C.

Figure 3- 7 reveals that multiple combinations of wavelengths can be applied to achieve small ΔQ for a given droplet diameter. For example, for a droplet diameter of 6 μm and a λ_3 of 5 μm, either a λ_4 near 5 or 3 μm results in small ΔQ. These wavelength combinations can be divided into two categories. The first category is a combination of two wavelengths close to each other (i.e. λ_3 = 5 μm and λ_4 close to 5 μm in the above example), and the second is a combination of two wavelengths well separated from each other (i.e. λ_3 = 5 μm and λ_4 close to 3 μm in the above example). However, the second

category of wavelength combinations is only applicable to cases with small droplet size changes. As shown in Figure 3- 7, when droplet diameter changes from 6 to 3 μm, ΔQ increases by a large amount if λ_4 is well separated from λ_3, while small ΔQ is maintained if λ_4 is close to λ_3. Mathematical considerations of the dependence of Q on droplet size and wavelength validate the generalization of above observations. Therefore, in general, wavelengths for vapor measurement by differential absorption must be close to each other for applications with varying droplet size.

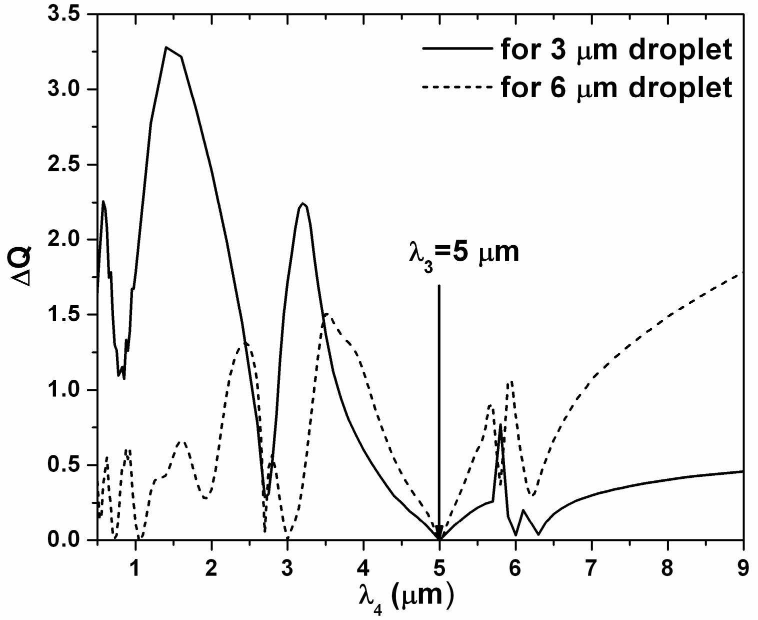

Figure 3- 7. ΔQ for water droplet with different diameters when λ_3 is selected at 5 μm.

Next, we consider the dependence of differential vapor absorption ($\Delta\tau_{vapor}$) on selected wavelengths (λ_3 and λ_4) with the goal of maximizing differential vapor absorption. Apparently, maximum differential absorption is achieved by selecting one wavelength (e.g. λ_3) where the strongest vapor absorption occurs and another wavelength (e.g. λ_4) where the weakest vapor absorption occurs over the entire spectral range of interest. For the example of water as shown in Figure 3- 6, one wavelength (λ_3) can be at a vapor absorption peak near 2.7 or 5.9 μm. Part a) of Figure 3- 8 shows the selection of λ_3 at 2.6705 μm, where maximum vapor absorbance occurs in the 2.5 to 3.0 μm spectral range. For the case with varying droplet size, which is of major interest to this work, the second wavelength (λ_4) must be close to λ_3. Part b) of Figure 3- 8 shows water vapor spectra in the vicinity of 2.6705 μm. In principle, a λ_4 chosen to be as close to λ_3 as possible provided that vapor does not absorb at this wavelength can minimize $\Delta\tau_{drops}$ while maintaining maximum $\Delta\tau_{vapor}$. A λ_4 of 2.6720 μm as shown in part b) of Figure 3-8 is an example of such a choice. But in practice, other considerations such as avoiding interference from pressure broadening of the vapor spectra, may encourage a different selection of λ_4, for example, 2.6818 μm as shown.

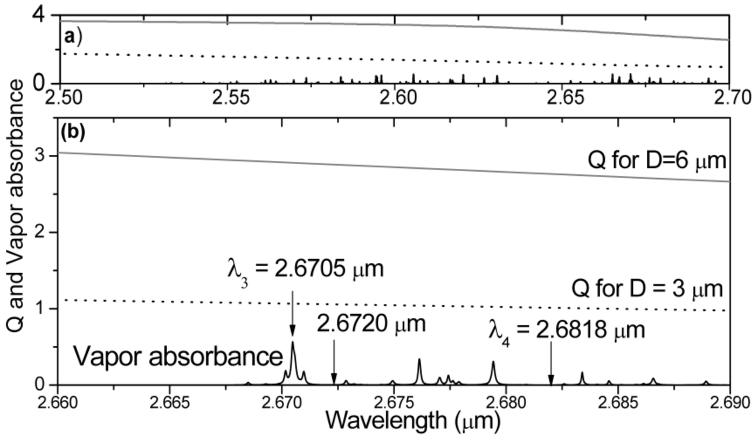

Figure 3- 8. Wavelength selection of differential absorption scheme for water with a temperature of 22^{0}C, total pressure 1 atm, mole fraction of water vapor 3%, and pathlength of 1cm.

Finally, we evaluate the applicable range of the above differential scheme for water vapor detection in an evaporating spray. Here we consider a system of water aerosols bathed in an inert gas undergoing uniform evaporation at constant pressure (1 atm) and temperature (22^0C), as a simplified model of the aerosol evaporation behind shock waves [64]. The system starts at time=0 with all droplets at diameter D_0, droplet volume fraction C_{V0}, and no vapor. As time progresses, the diameter of the droplets (D) and the droplet volume fraction (C_V) decreases due to evaporation and, consequently, the mole fraction of water vapor in the system increases. The differential scheme designed above with λ_3 at 2.6705 and λ_4 at 2.6818 μm is applied to monitor vapor concentration. Comparison between $\Delta\tau_{drops}$ and $\Delta\tau_{vapor}$ during the evaporation process provides an evaluation of the applicable range of this vapor sensing scheme in terms of droplet size (D), droplet loading (C_V), and mole fraction of vapor. This work uses the range where $\Delta\tau_{vapor}$ exceeds $\Delta\tau_{drops}$ to quantify the applicable range of the differential absorption scheme.

This comparison is complicated because it depends on both initial droplet diameter (D_0) and droplet volume fraction (C_{V0}). Comparison at some representative initial diameter is therefore used to provide an insight into the applicable range of the differential absorption scheme. One such representative diameter can be obtained by seeking a diameter to maximize differential droplet extinction ($\Delta\tau_{drops}$) in Equation (3.18) for a given combination of differential absorption wavelengths. This initial diameter, denoted as $D_0^{\max}$, results in maximum $\Delta\tau_{drops}$ at time=0 in the evaporation process. Furthermore, both mathematical considerations and numerical computations reveal that other initial diameters will yield similar or smaller $\Delta\tau_{drops}$ during the entire evaporation process compared to that yielded at $D_0^{\max}$. Therefore, comparison between $\Delta\tau_{drops}$ and

$\Delta\tau_{vapor}$ at $D_0^{\max}$ provides a lower limit of the applicable range of the differential absorption, i.e. the applicable range for other initial droplet diameters will be similar or wider than that evaluated at $D_0^{\max}$. For the differential scheme shown in Figure 3- 8 (λ_3 at 2.6705 and $\lambda 4$ at 2.6818 μm), $D_0^{\max}$ is found to be 5.1 μm. Therefore, the range where $\Delta\tau_{vapor}$ exceeds $\Delta\tau_{drops}$ evaluated at $D_0^{\max}$=5.1 μm represents a lower limit of the applicable range of this differential absorption scheme, and this scheme can be applied for vapor detection in a wider range at other D_0's .

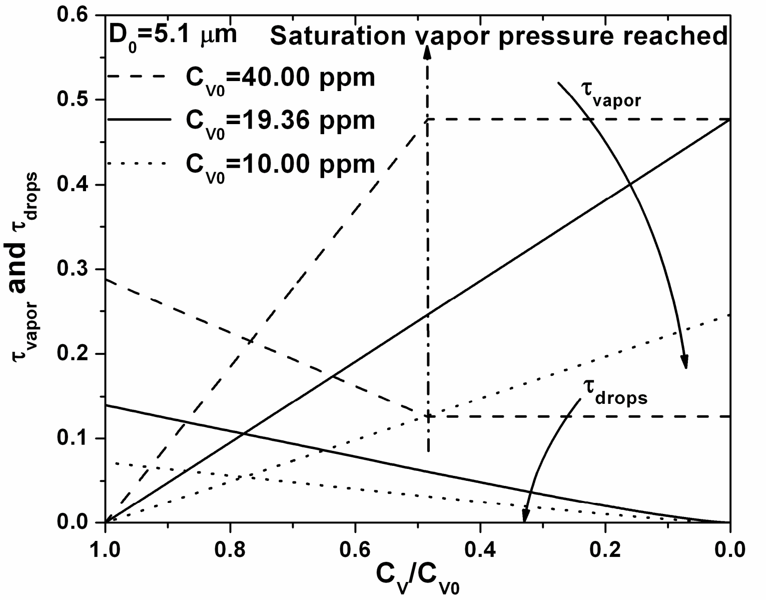

Figure 3- 9. Comparison of droplet extinction and vapor absorption at a wavelength of λ_3=2.6705 μm for the evaporation process depicted in Figure 3- 10 to evaluate the applicable range of single wavelength scheme for vapor detection. Evaluation performed at a temperature of 22^0C, pressure 1 atm, and pathlength of 1 cm.

Vapor absorption and droplet extinction at a single wavelength (λ_3=2.6705 μm) are first calculated in Figure 3- 9 for a few initial droplet volume fractions at D_0=5.1 μm. Note a C_{V0} of 19.36 ppm (parts per million) corresponds to the case that the saturated water vapor pressure at the given temperature is reached when all the droplets in the system are evaporated. Therefore, at a C_{V0} higher than 19.36 ppm (for example 40 ppm), the saturated water vapor pressure is reached when the droplets are only partially evaporated (about 50% evaporated in the example of C_{V0}=40 ppm), and vapor absorption becomes a constant afterwards. Figure 3- 9 suggests that accurate vapor measurement by single wavelength is jeopardized by large droplet extinction interference for some range of droplet volume fraction while vapor absorption itself is strong enough to allow accurate vapor measurement. For example, for the case when C_{V0}=40 ppm, after about 10% of the droplets are evaporated, the vapor absorbance reaches about 10% and accurate vapor detection can be readily performed at this absorbance level. However, droplet extinction imposes significant interference on vapor detection because τdrops exceeds τ_{vapor} by almost a factor of three at this stage of evaporation as shown in Figure 3- 9. Once at least 22% of the droplet volume evaporates (i.e. C_V/C_{V0}<78%), τ_{vapor} starts to exceed τ_{drops}, and this single wavelength detection scheme becomes applicable afterwards by the definition in this work.

The differential absorption strategy extends the vapor measurement into the range where strong interference from droplet extinction impairs the utility of single wavelength detection. Figure 3- 10 shows the comparison between $\Delta\tau_{drops}$ and $\Delta\tau_{vapor}$ when the differential scheme (λ_3 at 2.6705 and λ_4 at 2.6820 μm) is applied to the evaporating process described above. Obviously, $\Delta\tau_{vapor}$ starts to exceed $\Delta\tau_{drops}$ much earlier in the process than τ_{vapor} starts to exceed τ_{drops} in Figure 3- 9, therefore, a wider domain of accurate vapor detection is achieved using differential absorption. In the case shown in Figure 3- 10, vapor detection is limited by the magnitude of vapor absorption itself, not by interference from droplet extinction as in the case of Figure 3- 9. For example, for the case when C_{V0}=40 ppm, after about 2% of the droplets are evaporated (i.e. C_V/C_{V0}<98%), vapor absorbance starts to exceed droplet extinction and, therefore, the differential absorption scheme becomes applicable for vapor detection afterward. Although differential vapor absorbance is low (~1.5%) because the vapor concentration is low at this stage of evaporation, stronger differential signal can be achieved by utilizing a longer pathlength. Note that a D_0 of 3.0 μm results in smaller $\Delta\tau_{drops}$ than that from a D_0 of 5.1 μm, as expected. Also note that the applicable range of differential absorption is not strongly sensitive to normalized droplet volume fraction (i.e. C_V/C_{V0}) from Figure 3- 10.

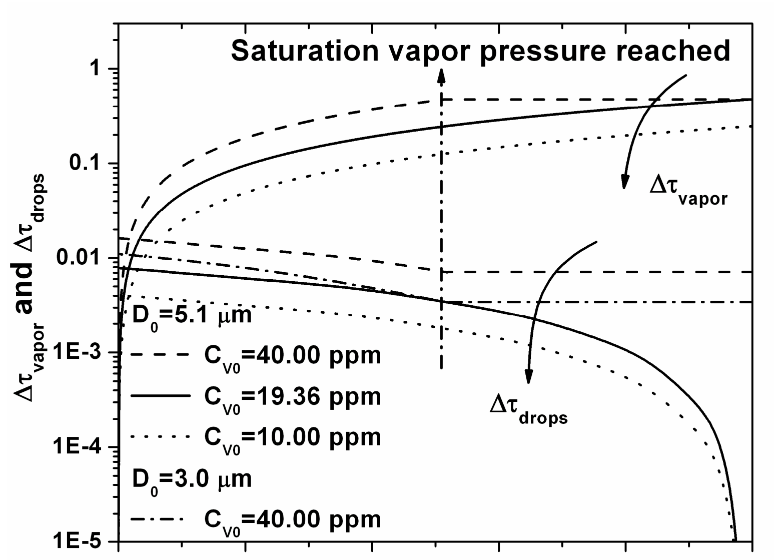

Figure 3- 10. Comparison of differential droplet extinction and vapor absorption between the wavelengths chosen in Figure 3- 9 for the evaporation process depicted in Figure 3- 10 to evaluate the applicable range of the differential absorption scheme for vapor detection. Evaluation performed at a temperature of 22^{0}C, pressure 1 atm, and pathlength of 1 cm.

3.5.3 Differential Absorption and Wavelength Availability

Discussions in Section 3.5.2 are based on the assumption that light sources are available at any wavelength to allow the utilization of the strongest differential vapor absorption. Although the strongest differential vapor absorption cannot be always accessed in practice due to the lack of light sources at proper wavelengths, it can be shown that differential absorption always extends vapor detection into wider domain compared with the single wavelength technique. Major conclusions about wavelength selection are transferable to other droplet/vapor systems than water and the methodology demonstrated above can be used evaluate the applicable range of specific differential absorption scheme. For example, currently there are no convenient and economical laser devices to provide the wavelengths near 2.67 μm shown in Figure 3- 8, but diode laser sources are readily available to access the absorption spectra by water vapor near 1.39 μm, where the strongest absorption of the $\upsilon_1+\upsilon_3$ band of water vapor occurs. Though the absorption from water vapor near 1.39 μm is weaker than that near 2.67 μm by about an order of magnitude, a differential absorption scheme based on the absorption features near 1.39 μm still enables $\Delta\tau_{vapor}$ to start to exceed $\Delta\tau_{drops}$ in an early stage of evaporation in the process described above and, therefore, allows accurate vapor detection in a wide range of droplet loading and vapor concentration.

3.6 Summary

Design criteria and methods are developed for selecting the optimum wavelengths for simultaneous droplet size and vapor concentration in sprays. These criteria and methods are applied to the design of a sensor for water aerosols and water vapor measurements. The expected performance of the sensor is simulated for an evaporating spray containing both droplet and vapor to support application for temporally-resolved measurements. These results demonstrated that the new sensing technique significantly extends the applicable range of extinction and absorption methods, in terms of the range of the droplet size, number density of the droplets, and concentration of the vapor. This work provides a systematical summary of the theory for simultaneously measuring droplet/vapor based on laser extinction, and is expected to lay the groundwork for implementing optical sensors based on WMLE in a variety of research and industrial applications involving multi-phase flows.

3.7 Acknowledgement

Part of this research was conducted under the advisory of Professor Ronald K. Hanson at Stanford University. I want to thank Professor Hanson for his guidance and support during the course of this work.

Chapter 4: Investigation of Temperature Parallel Simulated Annealing for Optimizing Continuous Functions with Application to Hyperspectral Tomography

4.1 Abstract

The simulated annealing (SA) algorithm is a well-established optimization technique which has found applications in many research areas. However, the SA algorithm is limited in its application due to the high computational cost and the difficulties in determining the annealing schedule. This paper demonstrates that the temperature parallel simulated annealing (TPSA) algorithm, a parallel implementation of the SA algorithm, shows great promise to overcome these limitations when applied to continuous functions. The TPSA algorithm greatly reduces the computational time due to its parallel nature, and avoids the determination of the annealing schedule by fixing the temperatures during the annealing process. The main contributions of this paper are

threefold. First, this paper explains a simple and effective way to determine the temperatures by applying the concept of critical temperature (T_C). Second, this paper presents systematic tests of the TPSA algorithm on various continuous functions, demonstrating comparable performance as well-established sequential SA algorithms. Third, this paper demonstrates the application of the TPSA algorithm on a difficult practical inverse problem, namely the hyperspectral tomography problem. The results and conclusions presented in this work provide are expected to be useful for the further development and expanded applications of the TPSA algorithm.

4.2 Introduction

The simulated annealing (SA) algorithm was first introduced in 1983 for solving combinatorial optimization problems [15]. Since then, it has been extensively studied, with successful demonstrations of its use for both discrete [16, 17] and continuous optimization problems [18-23]. These past research efforts have shown several critical advantages of the SA algorithm over other optimization techniques. For example, it can optimize complicated problems with a large number of variables and numerous confusing local minima. In addition, the SA algorithm is insensitive to the initial guess, which is especially important when no *a priori* information about the solutions is available.

On the other hand, the disadvantages of the SA algorithm are also well-recognized. One of the primary disadvantages of the SA algorithm is its high computational cost [20, 23]. Many research efforts that have focused on developing variants of the SA algorithm to reduce the computational cost [24-26] can be divided into two categories. Efforts in the first category attempt to optimize the annealing schedule [16, 27-30]. However, the optimal annealing schedule is usually problem-dependent [27, 28], therefore limiting the applicability of the results from these efforts. The second category involves the parallelization of the SA algorithm [25, 31-34]. However, most of these parallelization schemes do not guarantee convergence. Some of the parallelization schemes that do guarantee convergence, (e.g., the speculatively parallelized SA (SPSA) algorithm [33, 34]) can only achieve a maximum speedup efficiency of $\log_2(N_{proc})$, where N_{proc} is the number of processes used to implement the parallel algorithm.

The above considerations motivate the study of the temperature parallel simulated annealing (TPSA) algorithm which combines the well-established parallel tempering (or replica exchange) method [35, 36] and the SA algorithm [37]. The TPSA algorithm is another parallel SA algorithm that has theoretically been proven to be convergent [25, 32, 38], while being able to achieve linear speedup. In addition, optimization processes occur at constant temperatures in the TPSA algorithm; therefore, the TPSA algorithm does not require an annealing schedule. Once the starting and ending temperatures (T_0 and T_N) are determined, the remaining temperatures can easily be obtained. However, the TPSA algorithm has only been studied primarily on discrete functions in previous efforts [16, 32, 33, 37, 39]. Therefore, it is the goal of this current work to conduct a systematic study of the TPSA algorithm on continuous functions. This paper first explains a simple and effective way to determine T_0 and T_N by applying the concept of critical temperature (T_C) which has been successfully demonstrated on various complicated functions in [19]. Then systematic tests of the TPSA algorithm on various continuous functions are reported, demonstrating comparable performance as well-established sequential SA algorithms.

The above studies are directly motivated by a practical application, in which a so-called hyperspectral tomography problem is desired to be solved efficiently to obtain *in situ* measurements of the temperature and concentration of chemical species [8, 9]. Therefore, the application of the TPSA algorithm developed in this paper was also applied to solve the hyperspectral problem, illustrating its usefulness and potential for practical applications.

The remainder of this paper is organized as follows. Section 4.3 provides a detailed introduction to the TPSA algorithm. Section 4.4 discusses the determination of the T_0 and T_N using the concept of T_C, while Sections 4.5 and 4.6 evaluate the performance of the TPSA algorithm in terms of accuracy and computational time. Section 4.7 discusses the impact of other parameters important to the TPSA algorithm, including the relationship between the speedup efficiency and the number of processes (N_{proc}), and the effects of the exchange frequency (EF). Section 4.8 describes the application of the TPSA algorithm to a practical problem, where the TPSA algorithm was applied to perform tomographic inversion of hyperspectral measurements. Finally, Section 4.9 summarizes the paper.

4.3 Temperature Parallel Simulated Annealing

The TPSA algorithm, a parallel implementation of the SA algorithm, offers two advantages over sequential SA algorithms: 1) the determination of the annealing schedule can be avoided by fixing the temperatures as constant throughout the optimization process, and 2) a reduction in computational time can be achieved. Note that under the context of the SA algorithm, the term *"temperature"* represents a *parameter* used in the algorithm, to be differentiated from the physical temperature to be measured in the hyperspectral tomography technique later in Section 4.8 of the paper.

The mechanism of the TPSA algorithm has been explained elsewhere under the context of combinatorial optimization [16, 32], and is illustrated in Figure 4- 1 and briefly summarized here. First, N+1 temperatures (T_0 to T_N) are generated and dispatched to N+1 processes. Then, each process performs an optimization procedure using a sequential SA algorithm with the assigned temperature fixed as constant. Here, a well-established sequential SA algorithm described in [20] is used. After a pre-set number of iterations on each process, the processes with adjacent temperatures (labeled as T and T' in Figure 4- 1) exchange their optimal solutions as shown in Figure 4- 1. The exchange occurs at a probability p as defined in Figure 4- 1. If the solution at the higher temperature exhibits a smaller function value than that of the lower temperature, the solutions are always exchanged. Otherwise, the solutions will be exchanged with a probability less than 1. The specific value of the probability is determined by the temperature difference between *T* and *T'* (labeled as *ΔT*) and the difference in the functional values (labeled as *Δf*).

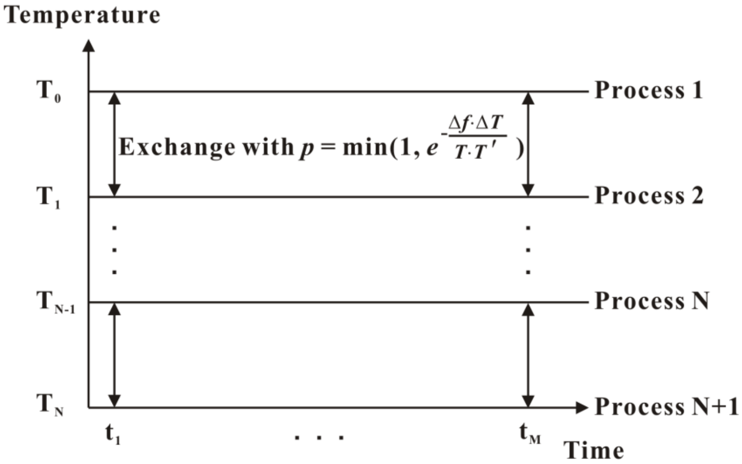

Figure 4- 1. Illustration of the TPSA algorithm.

This procedure of exchanging solutions starts from the processes with the two highest temperatures and proceed to those with the two lowest temperatures. Therefore, the downward direction of the exchange tends to concentrate the solutions with smaller function values at lower temperatures, where further reduction in function values is more likely to occur and to converge. However, meanwhile, it also becomes less likely to escape local minima at lower temperatures. This issue is solved by the upward direction of the exchange, where the local minima at lower temperatures can be transferred to higher temperatures, allowing the TPSA algorithm to escape the local minima and find the global minimum.

One important parameter involved in the above procedure is the frequency of the exchange, *EF*. This paper defines the *EF* as follows:

$$EF = \frac{1}{N_{step}^{adj}} \tag{4.1}$$

where N_{step}^{adj} is the number of the step-length adjustments before each solution exchange. See [20] for more details about the adjustment of the step-length in the sequential SA. This paper defines the following quantity, ΔF, to quantify the performance of optimization:

$$\Delta F = F - F_{global} \tag{4.2}$$

where F is the minimum value of the target function obtained, and F_{global} the global minimum of the target function. Obviously, a ΔF of zero means the algorithm has found the global minimum; and a smaller ΔF means the algorithm has approached a solution that is closer to the global minimum.

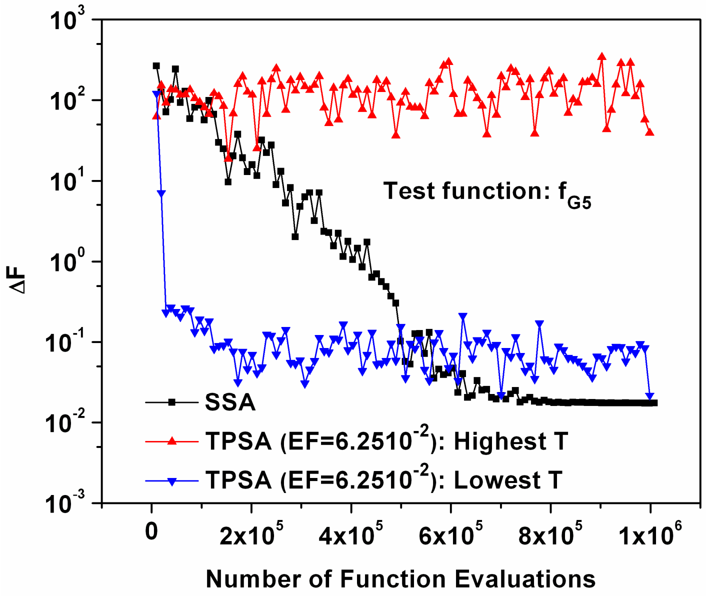

Figure 4- 2. Evolution of ΔF for both the SSA and TPSA algorithms.

Figure 4- 2 compares the typical behaviors of the TPSA algorithm and the sequential SA (SSA) algorithm. The function used here is the Griewangk's function with 5 variables (a detailed description of the function is provided in the appendix). The same number of function evaluations was used in both algorithms. For the SSA algorithm, the ΔF is recorded each time the temperature is reduced. For the TPSA algorithm, the ΔF is recorded each time the solutions exchange. As shown in Figure 4- 2, the ΔF of the SSA exhibits a decreasing trend as the algorithm proceeds, illustrating the convergence of the algorithm. The fluctuations in ΔF illustrate the algorithm's ability to escape local minima. In contrast, the ΔF of the TPSA algorithm oscillates around certain values. More specifically, the ΔF at the highest temperature (T_0) oscillates around a higher value, illustrating the upward direction of the exchange; and the ΔF at the lowest temperature around a lower value, illustrating the concentration of smaller function values towards lower temperature.

4.4 Determination of Starting and Ending Temperatures

The starting and ending temperatures, T_0 and T_N, are critical parameters for the TPSA algorithm. If T_0 is too high, the algorithm will not be efficient because the upward exchange will almost always be accepted at high temperatures. On the other hand, if T_0 is too low, the algorithm will be unable to escape local minima because the probability for upward exchange diminishes. For similar reasons, the TPSA algorithm will be unable to converge to the global minimum if T_N is too high, and will suffer low efficiency if T_N is too low. The authors of [16] presented a method to determine these two temperatures by utilizing the Genetic Algorithm (GA). The authors tested their method on combinatorial problems [16] and observed encouraging results. However, it has been noted that incorporating the GA further complicates the optimization algorithm by requiring elaborate parameter tuning [75]. Other authors suggested adaptive T_0 and T_N by maintaining empirically determined acceptance ratio [76], which also complicates the implementation of the algorithm. This work, therefore, seeks an alternative simple approach to determine the T_0 and T_N.

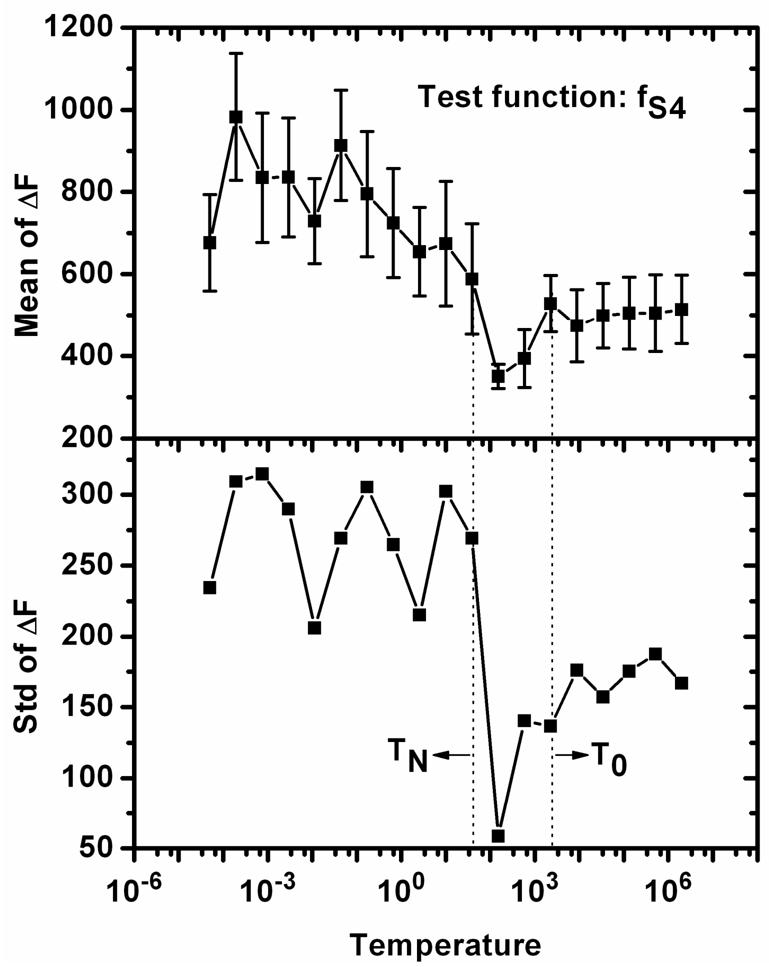

Figure 4- 3. Determination of T_0 and T_N using the T_C-curve.

The critical temperature, T_C, is an important and useful concept in the SA algorithm. It has been found that the SA algorithm explores the searching space more efficiently at T_C than at other temperatures [27, 29, 30]. A recent work has examined the application of T_C in minimizing continuous functions using sequential SA algorithms [19]. Here, we found that the use of T_C is also effective in determining the starting and ending temperatures for the TPSA algorithm. As to be discussed in Sections 4.5 and 4.6, using the starting and ending temperatures determined by T_C, the TPSA algorithm provides comparable performance to well established SSA algorithms.

Figure 4- 3 illustrates the concept of T_C, using the Schewefel's function with 4 variables, which is denoted as f_{S4}. A detailed description of this function and the method to generate the results shown here can be found in [19]. Briefly, the SSA algorithm was conducted independently at 10 constant temperatures ranging from ~10^{-5} to ~10^{6}. At each temperature, 10 cases were performed and the mean value and standard deviation (std) of the ΔF's were recorded. The top panel of Figure 4- 3 shows the mean value of the ΔF's with the error bar representing the std of the ΔF's, while the bottom panel shows the std. The results shown in Figure 4- 3 clearly illustrate that the SA algorithm exhibits three distinct behaviors at different temperature regions. First, when the temperature is high ($>10^5$), the output from the algorithm is characterized by a large ΔF and std. The reason for this behavior is that when the temperature is sufficiently high, the SA algorithm essentially samples the function randomly, resulting in high ΔF and std. Second, when the temperature is sufficiently low ($<10^0$), the algorithm essentially samples the local minima of the function randomly because the algorithm cannot escape a

local minimum once the algorithm enters one, resulting in high ΔF and std again. Third, in the temperature range of ~ 10^2 to 10^4, the results are characterized by both small ΔF and std. This paper names the temperature at which the smallest std of ΔF's occurs as T_C (T_C~10^3 for the f_{S4} function), and the curve shown in the lower panel of Figure 4- 3 the T_C-curve. It has been shown that, in the region near T_C, the SA algorithm has a high probability of locating the global minimum for various problems with complicated energy landscapes as demonstrated in [19].

Here, we use the T_C-curve generated as described above to determine the starting and ending temperatures for the TPSA algorithms. Specifically, the starting and ending temperatures are chosen to be the temperature immediately higher and lower than T_C, respectively, as shown on the T_C-curve. The effectiveness of this simple scheme will be demonstrated in Sections 4.5 and 4.6.

4.5 Evaluation of Performance

To evaluate the performance of the TPSA algorithm and the effectiveness of the scheme for determining T_0 and T_N, a TPSA algorithm was implemented in FORTRAN 90 and compared to a well-established SSA algorithm [20]. Note that there are also other variations of the SSA algorithms [10, 11], and it would be interesting to examine which SSA algorithm is optimal for parallelizing under the TPSA scheme. However, such an examination is out of the scope of this current work, and merits a full-length paper by itself. Therefore, in this work, we chose to work with a well established SSA algorithm

[6]. In the SSA, a relative change of function values (ε_{SA}=10^{-6}) during two consecutive temperature reductions was used as the termination criterion. Two measures were taken to make the results comparable. First, both algorithms are performed using the same number of function evaluations. More specifically, the SSA algorithm was run using the parameters recommended in [20] and the aforementioned stop criteria of ε_{SA}=10^{-6} was implemented. Upon the termination of the SSA algorithm, the number of evaluations of the target function was recorded. Then the same number of function evaluations was assigned evenly across all the processes used in the TPSA algorithm. The TPSA algorithm was terminated when the number of function evaluations at each process reached its assigned quota. Second, a local search was performed at the end of the SSA and TPSA algorithms. The local search guarantees that the global minimum will be found if either algorithm can locate a solution near the global minimum. The local search used the quasi-Newton method with the termination criterion set as ε_{Local}=10^{-8}, where ε_{Local} is the relative change of function values between two consecutive function evaluations. The computational cost of the local search was less than 1% of SA evaluations in both the SSA and TPSA algorithms.

The comparisons were made on various functions, each representing a unique optimization challenge. For example, the Michalewicz's function with 10 variables (f_{M10}) has a global minimum hidden in a deep narrow valley buried among 10! ($\sim 3.6\times10^{6}$) local minima, and the Schwefel's function (f_{S8}) function has a global minimum far from the local minima. More details about these test functions can be found in the appendix of [19] and also in the appendix of this paper.

	Number of Function Evaluations	**SSA**	**TPSA ($EF=1$)**	**TPSA ($EF=6.25\times10^{-2}$)**	**TPSA ($EF=3.91\times10^{-3}$)**
f_{B2}	1.60×10^{4}	1.00×10^{-16}	1.00×10^{-16}	1.00×10^{-16}	1.00×10^{-16}
f_{G5}	1.25×10^{6}	2.91×10^{-14}	1.00×10^{-16}	1.00×10^{-16}	9.86×10^{-3}
f_{M2}	2.00×10^{5}	2.60×10^{-13}	5.11×10^{-14}	3.76×10^{-13}	4.22×10^{-13}
f_{M5}	1.00×10^{6}	2.70×10^{-11}	4.36×10^{-12}	4.76×10^{-12}	4.73×10^{-12}
f_{M10}	2.00×10^{6}	1.14×10^{-13}	2.74×10^{-11}	2.74×10^{-11}	1.45×10^{-11}
f_{Ra10}	2.50×10^{6}	6.48×10^{-12}	1.00×10^{-16}	8.88×10^{-15}	9.95×10^{-1}
f_{Ro5}	1.10×10^{6}	1.69×10^{-11}	2.67×10^{-10}	3.13×10^{-11}	1.18×10^{-10}
f_{S4}	1.00×10^{6}	7.40×10^{-3}	5.51×10^{-12}	5.29×10^{-12}	5.51×10^{-12}
f_{S8}	1.20×10^{6}	2.98×10^{0}	1.07×10^{-11}	1.01×10^{-11}	1.08×10^{-11}
f_{S12}	2.32×10^{6}	8.11×10^{-11}	1.61×10^{-11}	1.68×10^{-11}	1.73×10^{-11}

Table 4- 1. The best ΔF of SSA and TPSA on the Selected Test Functions

To compare the SSA and TPSA algorithms, a T_C-curve was generated for each of the test functions, from which the T_0 and T_N for the TPSA algorithm and the initial temperature for the SSA algorithm were determined. All computations were performed on two Dell workstations with dual Intel Xeon quad-core processors (X5482, 3.2 GHz). A set of results is listed in Table 4- 1 and Table 4- 2, and plotted in Figure 4- 4. The results are presented in terms of ΔF as defined before and also in terms of Δx as defined below to quantify the distance between the solution obtained and the true solution at the global minimum:

$$\Delta x = \left\| x - x_{global} \right\| \tag{4.3}$$

where x is the solution obtained from the SSA or TPSA algorithm, and x_{global} is the solution at the global minimum. For each function, 30 runs were performed using either the SSA or TPSA algorithm, with different random seeds. The best results from these 30 runs were selected and listed in Table 4- 1 and Table 4- 2, and also plotted in Figure 4- 4 for better visualization. The results from the TPSA algorithm are reported at three different *EF's* to illustrate the effects of exchange frequency.

	Number of Function Evaluations	**SSA**	**TPSA (*EF*=1)**	**TPSA (*EF*=6.25×10^{-2})**	**TPSA (*EF*=3.91×10^{-3})**
f_{B2}	1.60 x 10^{4}	3.06 x 10^{-10}	9.20 x 10^{-10}	4.35 x 10^{-10}	7.54 x 10^{-10}
f_{G5}	1.25 x 10^{6}	3.41 x 10^{-8}	2.93 x 10^{-9}	1.69 x 10^{-9}	6.28 x 10^{0}
f_{M2}	2.00 x 10^{5}	6.55 x 10^{-8}	4.53 x 10^{-8}	6.17 x 10^{-8}	5.75 x 10^{-8}
f_{M5}	1.00 x 10^{6}	2.43 x 10^{-7}	9.91 x 10^{-8}	1.63 x 10^{-7}	1.50 x 10^{-7}
f_{M10}	2.00 x 10^{6}	1.86 x 10^{-6}	2.63 x 10^{-7}	2.63 x 10^{-7}	2.42 x 10^{-7}
f_{Ra10}	2.50 x 10^{6}	7.43 x 10^{-6}	1.20 x 10^{-10}	7.19 x 10^{-11}	9.95 x 10^{-1}
f_{Ro5}	1.10 x 10^{6}	1.18 x 10^{-5}	2.51 x 10^{-5}	8.87 x 10^{-6}	2.01 x 10^{-5}
f_{S4}	1.00 x 10^{6}	5.44 x 10^{0}	7.16 x 10^{-7}	3.45 x 10^{-6}	3.94 x 10^{-6}
f_{S8}	1.20 x 10^{6}	1.72 x 10^{0}	1.61 x 10^{-6}	1.54 x 10^{-6}	3.04 x 10^{-6}
f_{S12}	2.32 x 10^{6}	4.82 x 10^{-7}	4.19 x 10^{-6}	8.20 x 10^{-6}	1.00 x 10^{-5}

Table 4- 2. The best Δx of SSA and TPSA on the Selected Test Functions

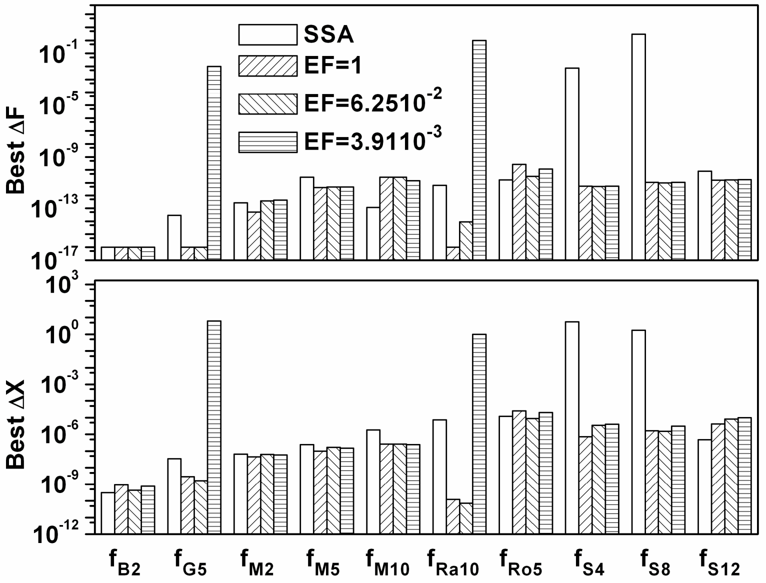

Figure 4- 4. Comparison of the SSA and TPSA algorithms on various test functions.

As shown by these results, at *EF*=6.25×10^{-2} and *EF*=1, the TPSA algorithm provides better or comparable performance both in terms of *ΔF* and *Δx* as the SA algorithm. Such performance across various test functions demonstrates the effectiveness of the TPSA algorithm for continuous functions and the method for determining T_0 and T_N using the T_C-curve. Also as shown by the results, the performance of the TPSA algorithm deteriorates as *EF* decreases. At an *EF* of 3.91×10^{-3}, the TPSA does not perform as well as the SSA algorithm on some of the test functions. More detailed discussions on the effects of the *EF* on the performance and computational cost are provided in Section 4.7.

4.6 Evaluation of Computational Cost

The previous section discussed the performance of the TPSA algorithm in terms of its accuracy, this section focuses on its computational cost.

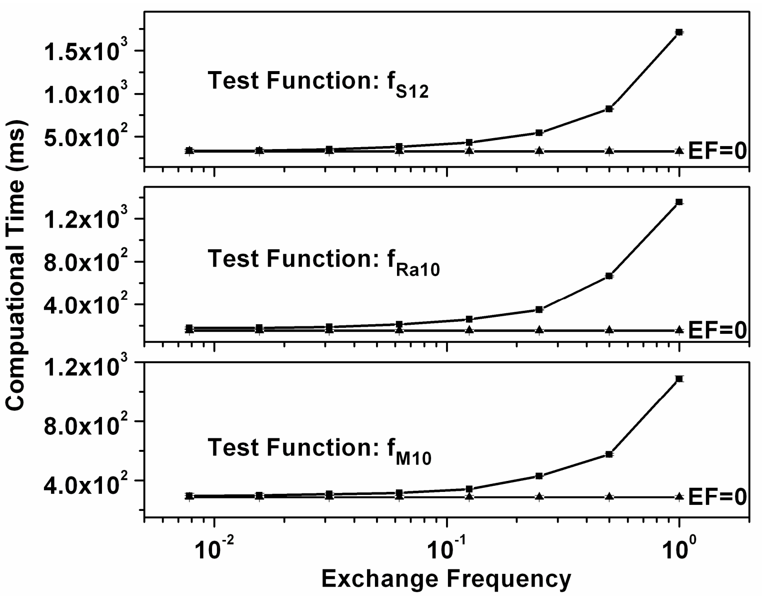

Figure 4- 5. Computational time of the TPSA algorithm as a function of the exchange frequency.

First, the effects of *EF* on the computational cost were examined. Figure 4- 5 illustrates the impact of the *EF* on the computational time of the TPSA algorithm. The TPSA algorithms at various *EF*'s ranging from ~10^{-2} to 1 are implemented using 16 processes and applied to 3 test functions, and the actual computational time (the wall-clock time) was recorded and plotted in Figure 4- 5. The same number of functions evaluations was (as determined by the method described at the beginning of Section 4.5) performed at each *EF* for each test function. As illustrated by these results, the computational time increases as *EF* increases, due to the computational overhead involved in evaluating the exchange criteria and in exchanging information between different processes. At an *EF*=1, the actual computational time was about 3× more than that at an *EF*=6.25×10^{-2}; and the benefits of such increased computational time were the improved performance as shown in Table 4- 1 and Table 4- 2. These computational times were also compared with the time when *EF* was set to zero. When *EF*=0, the

TPSA algorithm essentially reduces to a series of classic Metropolis algorithms, each running at a fixed temperature. The computational time in this case represents the time for actually evaluating the functions (i.e., without evaluating the exchange criterion and without communication between the processes). These times were shown on Figure 4- 5 by the straight lines labeled *EF*=0. The difference between the computational times at various *EF*'s and that at *EF*=0 represents the computational overhead in the TPSA algorithm due to exchanges.

Second, the effects of the number of processes (N_{proc}) on the computational cost were examined. Ideally, the computational time should exhibit a linear or super-linear dependence on N_{proc}. Here, to quantify the speedup efficiency of the TPSA algorithm, the following parameter (Φ) is defined:

$$\Phi = \frac{\text{Computational time of SSA}}{(\text{Computational time of TPSA}) \cdot N_{proc}} \tag{4.4}$$

where all the times are wall-clock time. Clearly, Φ indicates the efficiency of the parallel algorithm: $\Phi=1$ means a linear speedup, $\Phi>1$ a super-linear speedup, and $\Phi<1$ stands for a sub-linear speedup. Figure 4- 6 shows the relationship between Φ and N_{proc} at different *EF*'s for two test functions. The TPSA algorithm was implemented on various numbers of processes ranging from 2 to 64. At each N_{proc}, 30 test runs were conducted. The points in the figure represent the mean value of Φ for these 30 cases and the error bars the std. As Figure 4- 6 shows, the std is generally quite small (too small to be visible in many cases shown here), evidencing the repeatability of the runs.

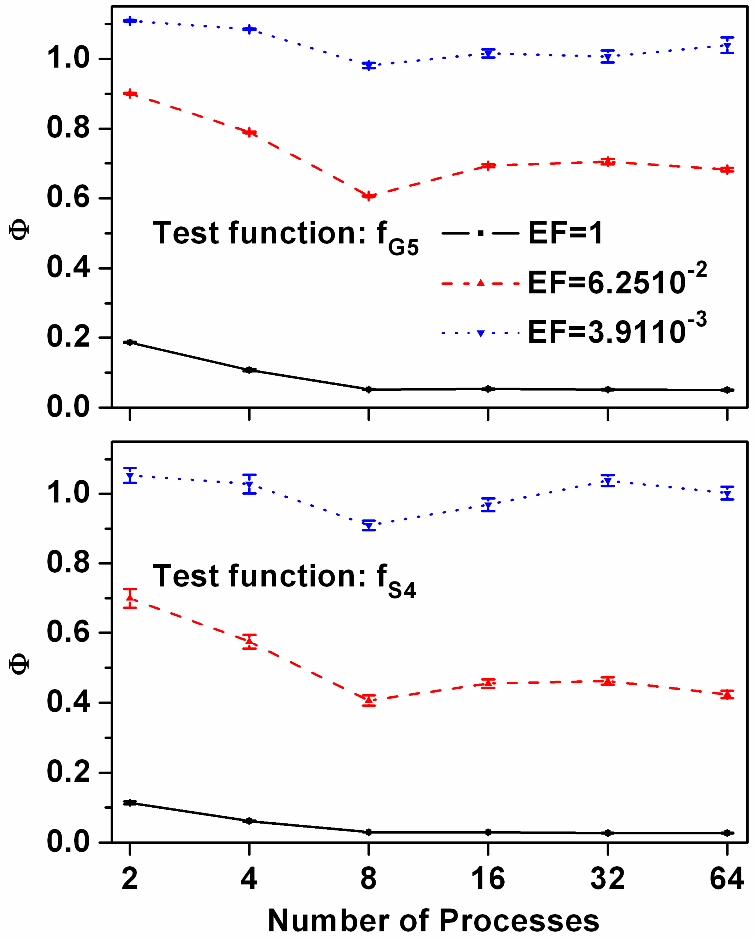

Figure 4- 6. The relationship between the speedup efficiency and the number of processes used in the TPSA algorithm.

As can be seen, a higher *EF* (corresponding to a larger computational overhead) results in a smaller Φ. At a specific *EF*, the Φ exhibits a weak dependence on N_{proc}, which might be due to the particular structure of our workstations. At an *EF* of 3.91×10^{-3}, a slightly super-linear speedup can be achieved for the range of N_{proc} tested. However, at large *EF*'s, the TPSA algorithm only enables sub-linear speedup, due to the increased overhead as shown in Figure 4- 5.

4.7 Preliminary Study of Exchange Frequency

The results reported in Sections 4.5 and 4.6 suggest that TPSA provides better performance at larger *EF*, at the cost of increased computational time. Therefore, it is highly desirable to have some insight into optimizing the tradeoff between the performance and computational time. Previous studies on such optimization have focused on discrete functions [16, 32], and have shown that the performance of the TPSA algorithm becomes insensitive to *EF* after a certain value. Here, we examined the dependence of the TPSA's performance on *EF* for continuous functions, and found that the pattern of the dependence is more complicated than for discrete functions.

Two representative patterns were selected and shown in Figure 4- 7 and Figure 4-8. In these figures, the TPSA algorithm was implemented on 16 processes to minimize various test functions, and 30 cases were run on each test function. The mean and std (represented by the error bar) of the ΔF obtained for these 30 cases were shown here. Figure 4- 7 shows the "normal" patterns, i.e., the performance of the TPSA improves as *EF* increases for the test functions shown in Figure 4- 7. This pattern is what one would intuitively expect: the algorithm should locate the global minimum more accurately if information across at different processes is exchanged more frequently. In contrast, the patterns shown in Figure 4- 8 are "abnormal", where the performance shows a weak or even fluctuating dependence on *EF*. As the top panel of Figure 4- 8 shows, for the f_{S4} function, the performance (again measured in terms of ΔF and its std) fluctuates with *EF*; and the bottom panel of Figure 4- 8 shows a weak dependence for the f_{Ro5} function.

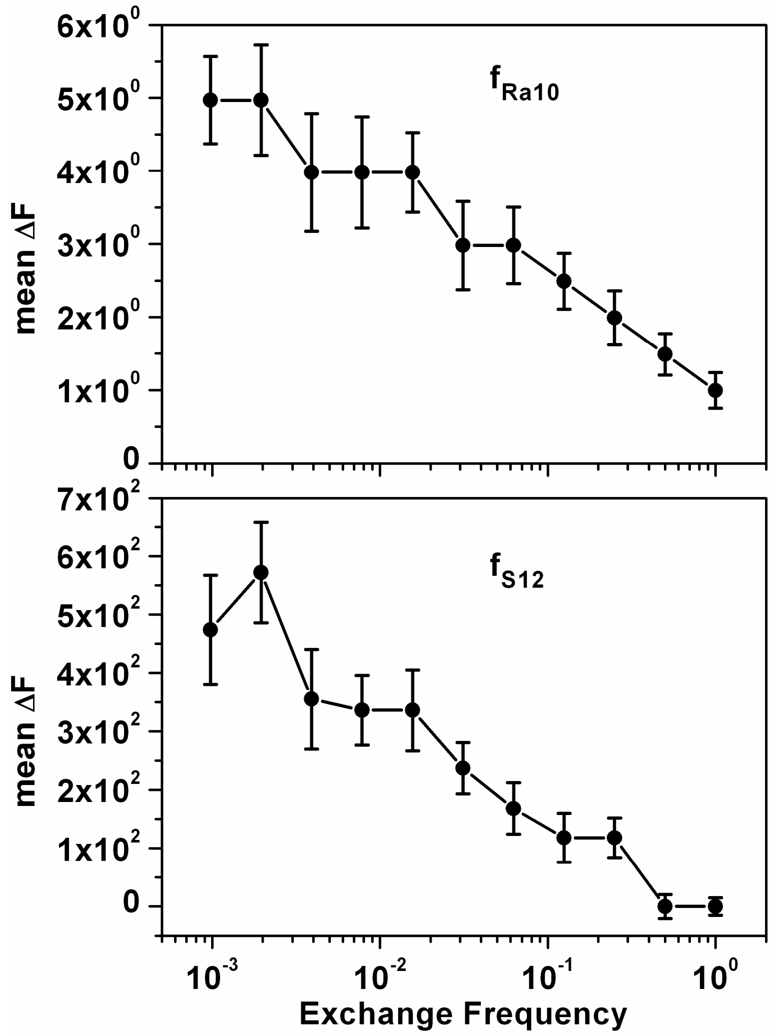

Figure 4- 7. Impact of the exchange frequency on the performance of the TPSA algorithm for the f_{Ra10} and f_{S12} functions.

Though the dependence of TPSA's performance on *EF* is complicated as discussed above and remains as on ongoing research direction, several preliminary observations can be made for optimizing the tradeoff between performance and computational cost. First, an *EF* larger than 6.25×10^{-2} already provided comparable performance to the SSA algorithm as shown in Table 4- 1 and Table 4- 2, and in Figure 4- 4. Also, TPSA's performance at an *EF* of 6.25×10^{-2} is only worse than at an *EF* of 1 marginally. Second, as Figure 4- 5 shows, the computational time at *EF*=1 is about 3×

more than that at *EF*~10^{-3} due to the increased computational overhead. Such overhead will decrease (relative to the computational time for evaluating the target function) when the target function becomes more expensive to evaluate, and many target functions in practice are considerably more expensive to evaluate than the test functions used here. Therefore, using an *EF*=1 might be a feasible practical strategy for many applications. Our results agree with the conclusion of [77], which also suggests low exchange frequency.

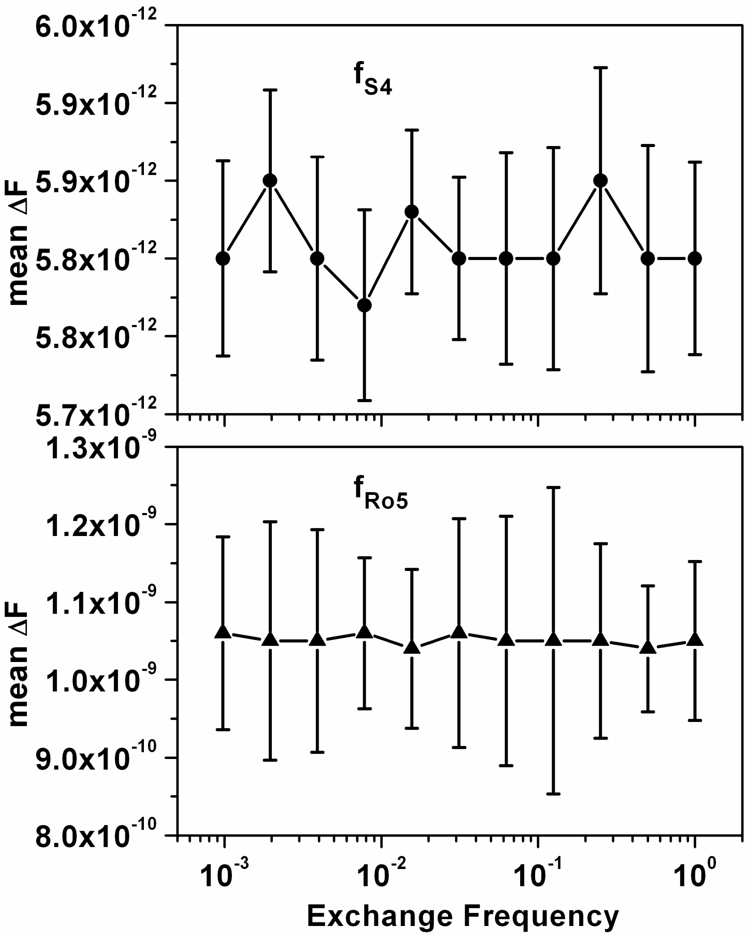

Figure 4- 8. Impact of the exchange frequency on the performance of the TPSA algorithm for the f_{S4} and f_{Ro5} functions.

4.8 Application to Hyperspectral Tomography

This section describes the application of the TPSA developed above in a so-called hyperspectral tomography (HT) problem. The goal of the HT problem is to image the distribution of the property of a chemical species (e..g, temperature or concentration) using of line-of-sight-integrated absorption measurements at various wavelengths. The HT problem is highly nonlinear and computationally intensive [4, 8, 9]. Thus there is a strong motivation to parallelize the solution of the HT problem, so that it can be solved quickly for *in situ* analysis.

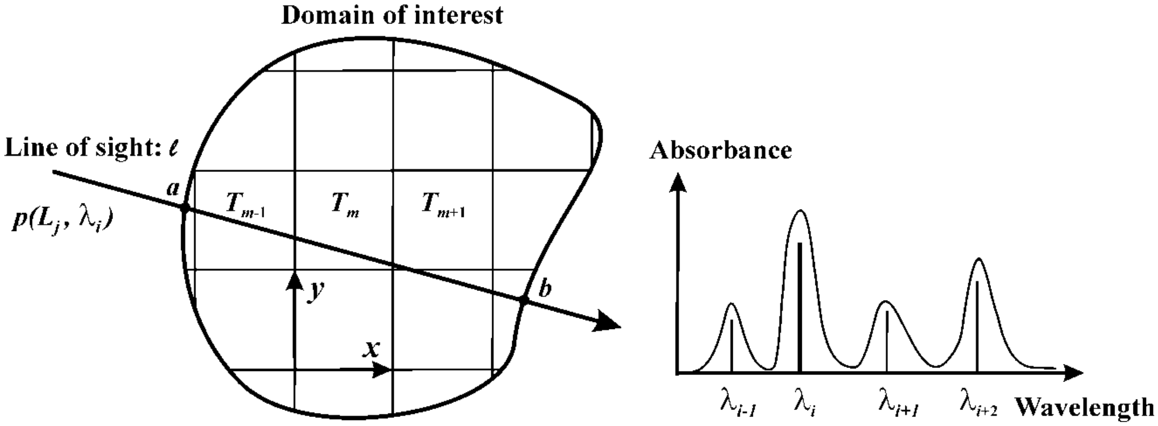

Figure 4- 9. The mathematical formulation of the hyperspectral tomography problem.

The mathematical background and experimental demonstration of the HT problem has been detailed in [4, 8] and [9], respectively. A brief summary is provided here for convenience. The configuration of the HT problem is illustrated in Figure 4- 9. A hyperspectral laser beam (i.e., a laser beam that scans a wide wavelength range) is directed along the line of sight, denoted by ℓ, to probe the domain of interest as shown in the left. Absorption by the target species will attenuate the probe laser beam, and the absorbance at a certain wavelength (e.g., λ_i) generally contains contributions from multiple transitions centered at various wavelengths (including that centered at λ_i itself), as schematically shown in the right. Here, we use $p(L_j, \lambda_i)$, termed a projection, to denote the absorbance at a projection location L_j and a wavelength λ_i. The projection, $p(L_j, \lambda_i)$, is expressed by the following integral:

$$p\left(L_j, \lambda_i\right) = \int_a^b \sum_k S\left(\lambda_k, T\left(\mathrm{l}\right)\right) \cdot X\left(\mathrm{l}\right) \cdot \Phi\left(\lambda_k - \lambda_i\right) \cdot P \cdot d\mathrm{l} \qquad (4.5)$$

where a and b the integration limits determined by the line of sight and the geometry of the domain of interest, $S(\lambda_k, T(l))$ is the line strength of the contributing transition centered at a wavelength λ_k and depends highly nonlinearly on temperature (T) [4]; $T(l)$ and X (l) the temperature and mole fraction profile of the absorbing species along the line of sight, respectively; Φ the Voigt lineshape function [9]; and P the pressure, assumed to be uniform. Note that the physical temperature (in unit of Kelvin) here is different from the "temperature" parameter used in the SA algorithms. The summation runs over all the transitions with non-negligible contributions, which compounds the computational intensity due to the significant overlap under practical conditions due to various broadening mechanisms. In this work, the domain of interest is discretized by superimposing a square mesh in the Cartesian coordinate, as shown in the left of Figure 4- 1**;** and the integration in Eq. (4.5) is also discretized accordingly.

With the above understanding, the hyperspectral tomography problem seeks to determine the distributions of T and X over the discretized domain with a finite set of projections as described in Eq. (4.5). Hence, mathematically, the hyperspectral tomography problem is an inverse problem, which has been studied extensively. However, due to the inclusion of multiple wavelengths and the nonlinear dependence of the line strength on temperature, the hyperspectral tomography problem poses distinct challenges and algorithms designed in the past cannot be readily applied. A new inversion algorithm was therefore developed to address the special challenges of the hyperspectral tomography problem [7, 8]. The algorithm casts the inversion problem into a nonlinear optimization problem, where the T and X distributions are retrieved by minimizing the following function:

$$D(T^{rec}, X^{rec}) = \sum_{j=1}^{J}\sum_{i=1}^{I}\frac{[p_m(L_j,\lambda_i) - p_c(L_j,\lambda_i)]^2}{p_m(L_j,\lambda_i)^2} \tag{4.6}$$

where $p_m(L_j, \lambda_i)$ denotes the measured projection at a location L_j and a wavelength λ_i; $p_c(L_j, \lambda_i)$ the computed projection based on a reconstructed T and X profile (denoted by T^{rec} and X^{rec}, respectively); and J and I the total number of wavelengths and projection locations used in the tomography scheme, respectively. However, the problem is a nonlinear optimization problem due to the nonlinear temperature-dependence of the line strength and the lineshape function; and typical minimization methods based on the derivatives (or gradients) of the objective function cannot be applied. These issues can be addressed, respectively, by 1) applying a regularization technique, and 2) using a stochastic minimization algorithm, the simulated annealing algorithm. More specifically, the following new target function (F) is minimized instead of D:

$$F(T^{rec}, X^{rec}) = D(T^{rec}, X^{rec}) + \gamma_T \cdot R_T(T^{rec}) + \gamma_X \cdot R_X(X^{rec}) \tag{4.7}$$

where R_T and R_X are the regularization factors for temperature and concentration, respectively; γ_T and γ_X are positive constants (regularization parameters) to scale the magnitude of R_T and R_X properly such that they do not dominate the $D(T^{rec}, X^{rec})$ term. The master function, F, is then minimized using the simulated annealing algorithm; and finally, the solution of the minimization problem described in Eq. (4.7) provides the tomographic reconstruction of the T and X distributions.

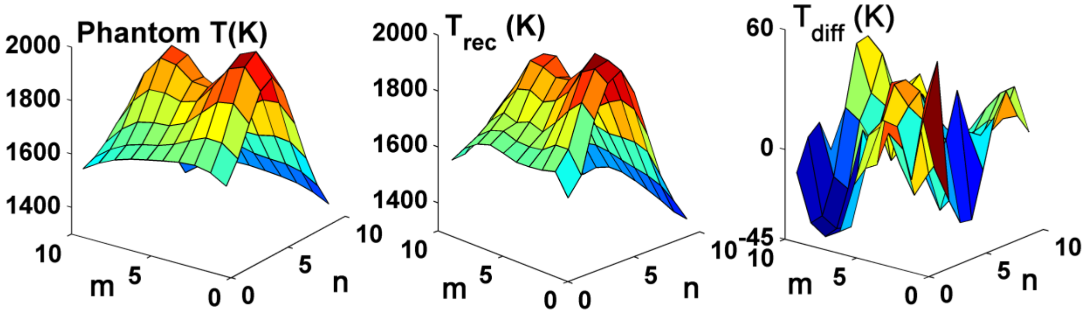

Figure 4- 10. Comparison of T phantom and reconstruction obtained using the TPSA algorithm.

Here, we applied the TPSA algorithm to the HT problem, demonstrating its comparable performance to previous techniques at reduced computational time. The left panel of Figure 4- 10 shows an example T phantom used in the study. The phantoms were generated over a 10-by-10 square grid by superimposing two Gaussian peaks on a paraboloid to simulate a representative multi-modal and asymmetric temperature distribution of H_2O in practical combustion devices. Other distribution phantoms have been tested and the results obtained are similar to those obtained with the phantoms shown here. A hypothetical HT sensor with 20 beams is applied to probe the distributions, with 10 beams probing in the horizontal direction and the other 10 in the vertical direction. Each beam contains 10 wavelengths, probing 10 different transitions of

H_2O. A set of simulated projections was then generated according to Eq. (4.5), and the TPSA algorithm was applied to solve the HT problem by minimizing Eq, (4.7). A reconstructed T distribution is shown in the mid panel, and the difference between the reconstruction and the phantom shown in the right panel. The inversion was performed on the Dell workstation with two Intel Xeon quad-core processors (X5482, 3.2 GHz) and eight processes was applied in the TPSA algorithm. We chose to conduct this study on such a workstation instead of on a large number of processors because the primary object is to examine whether it is feasible to process hyperspectral tomography data *in situ* on a small workstation or a PC. According to our computational experiments, the HT problem depends weakly on *EF* and the *EF* used here was chosen to be 0.125, considering the fact that the computation of the target function in Eq. (4.7) is considerably more costly than the exchange overhead. As these results show, the TPSA algorithm yielded reconstructions with high fidelity. In the example results shown here, the reconstruction error was within -40 K to 60 K and the overall reconstruction error was 1.56% (defined as error relative to the phantom averaged over all grids).

In comparison, Fig. 11 shows an example reconstruction using the sequential SSA algorithm [8]. The left panel shows the reconstruction, the mid panel shows the difference relative to the phantom, and the right panel shows the difference relative to the results obtained by the TPSA algorithm shown in Fig. 10. The overall reconstruction error was 1.59% in this case. The results in Fig. 10 and Fig. 11 demonstrated that the TPSA algorithm can achieve comparable reconstruction fidelity as the SSA algorithm.

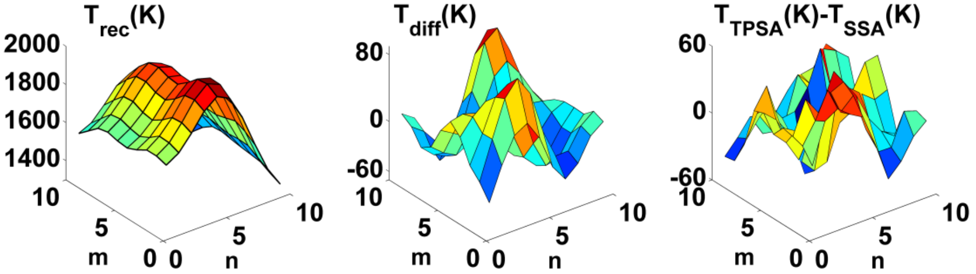

Figure 4- 11. Reconstruction obtained using the SSA algorithm in comparison to the phantom and that obtained using the TPSA algorithm.

Solving this example problem using the sequential SA algorithm required 430 seconds (~ 7 minutes) of computation time, and 102 seconds (~ 1.7 minutes) using the TPSA algorithm, representing around 4× reduction in computational time. The computation costs approximately scales linearly with the number of grids (i.e., a 20×20 case will require 4× more computation time than the 10×10 case). A 10×10 case represents a typical current hyperspectral tomography application because of two considerations. First, a 10×10 discretization is already sufficient for many practical applications; and second, a finer discretization poses implementation difficulty in practice in terms of optical access, laser power availability, etc. The processing time also varies approximately linearly with the number of wavelengths used, and the specific configuration of the workstation. A 1.7-minute processing time in our current study shows good promising of the TPSA for *in situ* analysis of HT measurements in many practical applications.

4.9 Summary

To summarize, this paper provides a systematic investigation of the TPSA algorithm on continuous functions, with application to a practical problem where tomographic reconstruction of a chemical species is obtained using hyperspectral absorption measurements. Two aspects of the algorithm were considered. First, this work developed a simple and effective way to determine the starting and ending temperatures for TPSA using the critical temperature. Second, this work conducted an extensive comparison of the TPSA algorithm against a well-established sequential SA algorithm, and demonstrated that comparable performance can be achieved. The results show that the TPSA algorithm is a reliable method which can achieve comparable performance to the SSA algorithm while greatly reducing the computational time. Implications of these findings are discussed under the context of the hyperspectral tomography problem. This work is expected to lay the groundwork for further development of the TPSA algorithm, and for its expanded applications.

4.10 Acknowledgements

Special thanks are due to Barbara Ramirez for her assistance in preparing the manuscript.

4.11 Appendix. Test Functions and Their Properties

This Appendix provides the definitions of the test functions and their properties. The definition of f_{G5} is as follows:

$$f_{G5} = \sum_{i=1}^{5} \frac{x_i^2}{4000} - \prod_{i=1}^{5} \cos(\frac{x_i}{\sqrt{i}}) + 1 \qquad -600 \le x_i \le 600 \tag{A.1}$$

The subscript "*G*" specifies that the test function is the Griewangk's function, and the subscript "5" refers to the number of variables in the function. The same notation rules are used for the other test functions. The numerous local minima of f_{G5} are regularly distributed. The function has its global minimum at $x_i = 0$ ($i = 1, 2, \ldots, 5$) and $F_{Global} = 0$, as illustrated in Figure 4- 12.

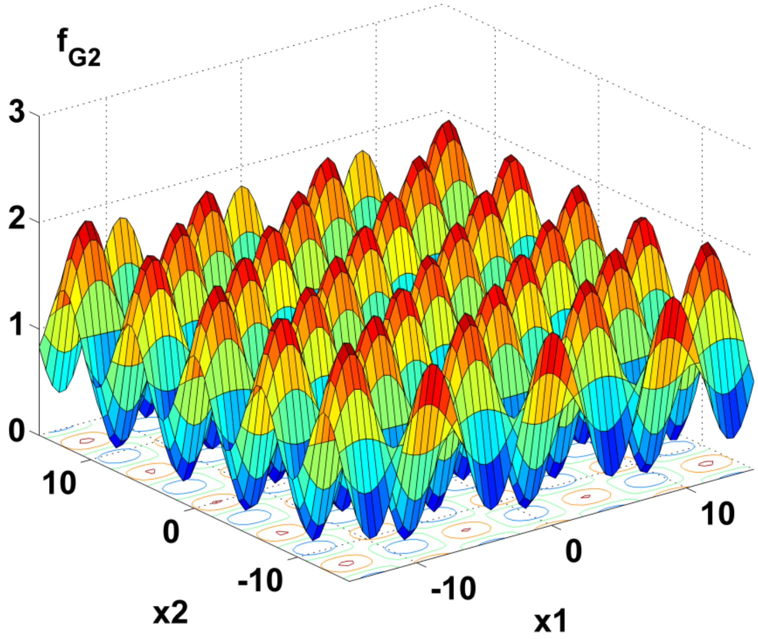

Figure 4- 12. A plot of test function f_{G5} with respect to the first two variables (the other three variables are set to zero).

The definition of f_{Ra10} is as follows:

$$f_{Ra10} = 100 + \sum_{i=1}^{10} (x_i^2 - 10 \cdot \cos(2 \cdot \pi \cdot x_i)) \qquad -5.12 \le x_i \le 5.12 \qquad \text{(A.2)}$$

The function has its global minimum at x_i =0 (i =1, 2, …, 10) and F_{Global} =0. This function shares similar features with f_{G5}, whose local minima are regularly distributed, as illustrated in Figure 4- 13.

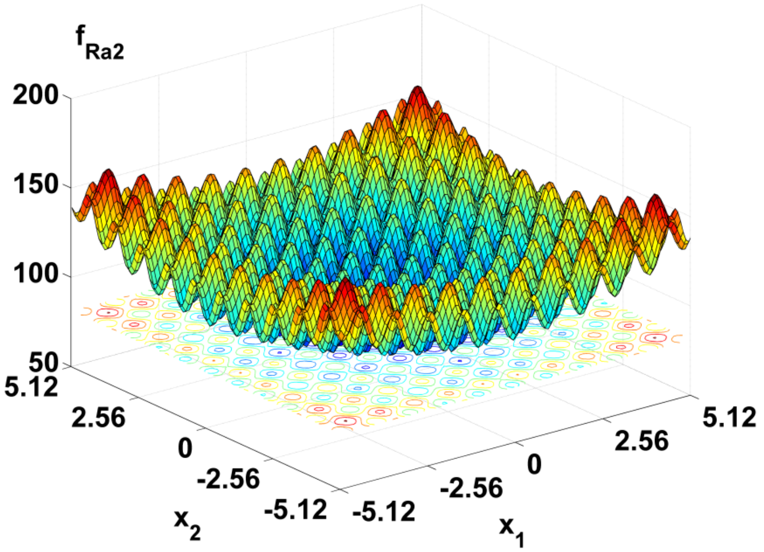

Figure 4- 13. A plot of test function *f_{Ra10}* with respect to the first two variables (the other variables are set to zero).

The next function, f_{B2}, is defined as:

$$f_{B2} = x_1^2 + 2x_2^2 - 0.3\cos(3\pi x_1) - 0.4\cos(4\pi x_2) + 0.7 \qquad -1 \le x_1, x_2 \le 1 \quad \text{(A.3)}$$

The global minimum of f_{B2} is at (0, 0) and F_{Global} =0. Figure 4- 14 shows a plot of test function f_{B2}, illustrating the many irregularly distributed local minima.

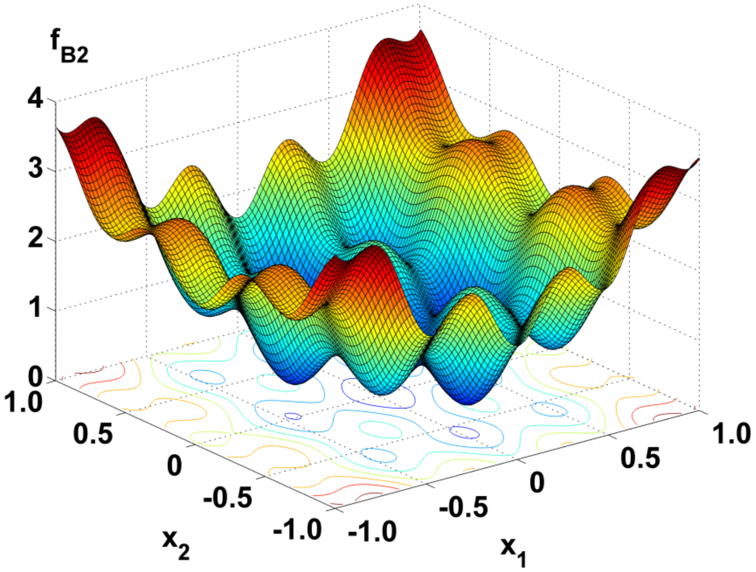

Figure 4- 14. A plot of test function *f_{B2}*.

The Michalewicz's function with *n* variables is defined as:

$$f_{Mn} = -\sum_{i=1}^{n} \sin x_i [\sin(\frac{i \cdot x_i^2}{\pi})]^{2m} \quad 0 \le x_i \le \pi \tag{A.4}$$

This function has a global minimum hidden in a deep narrow valley buried among *n*! local minima. The parameter *m* defines the sharpness of the valley containing the global minimum. Figure 4- 15 shows an example of the Michalewicz's function with five variables (*n*=5) with the first three variables set to zero), illustrating the large number of local minima and the steepness of the global minimum.

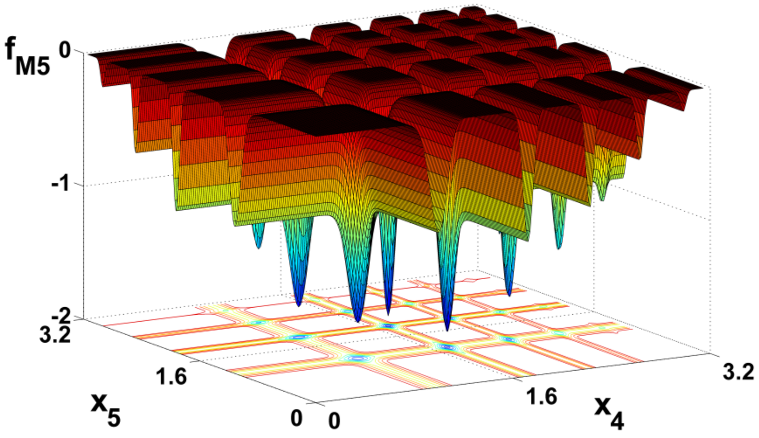

Figure 4- 15. A plot of test function f_{M5} with respect to the fourth and fifth variables (the first three variables are set to zero).

The Schwefel's function with n variables is defined as:

$$f_{Sn} = -\sum_{i=1}^{n} x_i \cdot \sin\sqrt{|x_i|} \qquad -500 \le x_i \le 500 \tag{A.5}$$

This function has its global minimum at x_i =420.9687 (i =1, 2, …, n) and F_{Global} =-418.9829·n. This function is characterized by a large number of local minima**,** which are widely separated from each other, as illustrated by the plot in Figure 4- 16 shows (n=2).

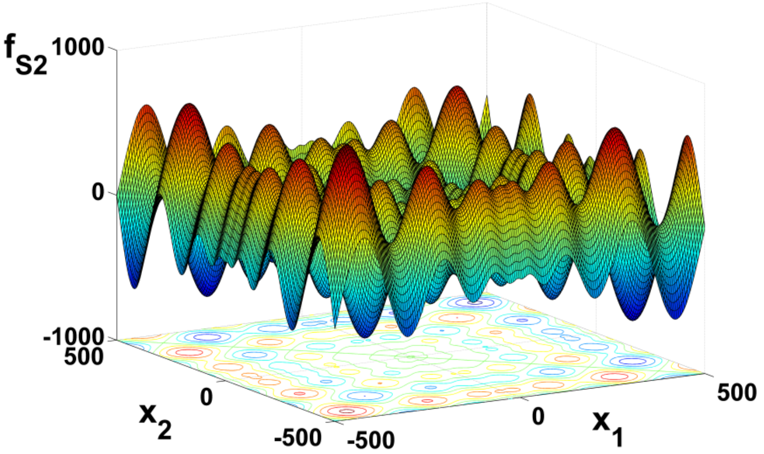

Figure 4- 16. A plot of the f_{S2} test function.

The last test function is the Rosenbrock's function (also known as the Banana function) with 5 variables. The Rosenbrock's function with n variables is defined as:

$$f_{Ron} = \sum_{i=1}^{n-1} 100 \cdot (x_{i+1} - x_i^2)^2 + (1 - x_i)^2 \quad -2.048 \leq x_i \leq 2.048 \qquad \text{(A.6)}$$

This function features a global minimum that is hidden inside a long and twisted flat valley. Finding the valley is trivial, however, navigating through the valley and locating the exact location of the global minimum is challenging. This function has a global minimum at x_i =1 (i =1, 2, …, 5) and F_{Global} =0. Figure 4- 17 shows a plot of the function with two variables, illustrating the shape and flatness of the valley, inside which the global minimum is located.

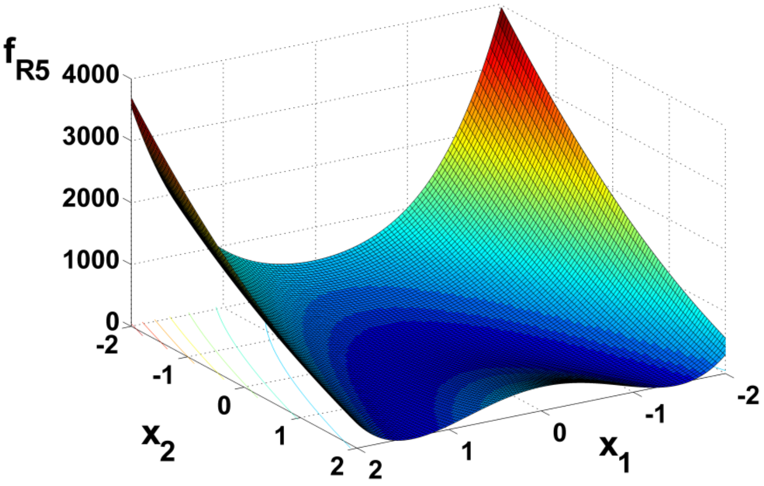

Figure 4- 17. A plot of the f_{R5} test function with respect to its first two variables (other variables are set to zero).

Chapter 5: Conclusion

In this final chapter, the results from this work are summarized from the studies of the application of PCMs, the development of a measurement technique for particles in multiphase environments, and the application of the TPSA algorithm to the data analysis. The latter two developments are expected to increase the understanding of the influence that nanoparticle sizing has on the thermal enhancements of nanofluids.

This work first investigated the practical application of selected phase change materials (PCMs) to a practical thermal management system for a LED headlight assembly. The major challenge was the fact that these organic PCMs, while possessing favorable latent heat properties, possessed very low thermal conductivities that would render any practical application of these materials not feasible. However, with the emergence of metal foams which can suspend these PCMs, the effective thermal conductivity can be increased to a level that is practical in a thermal management system. It is very clear that, for the system studied, PCMs show great promise in protecting the LED headlight system. PCMs provide delayed time to reach the failure temperature of these components and are easily integrated into this system without requiring additional energy input. Finally, an optimization process found the optimal volume fraction of the PCM that maximizes the operational time of the LED headlight assembly. These results should not only prove the applicability of using PCMs to protect the studied LED headlight system, but also demonstrate the applicability of using PCMs in many other systems needing enhanced thermal protection.

Next, in order to enhance the favorable characteristics of the PCM based thermal management system, this work investigated methods to measure the size of nanoparticles within a nanofluid in order to understand the effect that sizing has on the nanofluid. This study focused on developing a method to be applied to the multiphase flow problem of detecting the size of particles within a multiphase environment. The expected performance of the sensor is simulated.

Finally, this work endeavored to improve the inversion algorithm of the data by increasing the fidelity of solution while decreasing the computational time, which should prove valuable to the study of nanofluids. This work developed a new method based on simulated annealing for analyzing the data in a parallelized fashion (TPSA). By conducting an extensive comparison of the TPSA algorithm against a well-established sequential simulated annealing (SSA) algorithm, this work demonstrated that comparable performance can be achieved with reduced computation time. The results showed that the TPSA algorithm is a reliable method which can achieve comparable performance to the SSA algorithm while greatly reducing the computational time. Results of the TPSA algorithm given by this work are expected to lay the groundwork for further development of the detection of nanoparticles sizing characteristics in a nanofluid.

References

1. A. Pasupathy, R. Velraj, and R. V. Seeniraj, "Phase change material-based building architecture for thermal management in residential and commercial establishments," Renewable & Sustainable Energy Reviews **12,** 39-64 (2008).

2. M. M. Farid, A. M. Khudhair, S. A. K. Razack, and S. Al-Hallaj, "A review on phase change energy storage: materials and applications," Energy Conversion and Management **45,** 1597-1615 (2004).

3. D. L. Vrable, and K. L. Yerkes, "A thermal management concept for more electric aircraft power system applications," SAE Technical Paper Series **981289,** 1-6 (1998).

4. S. A. Khateeb, M. M. Farid, J. R. Selman, and S. Al-Hallaj, "Design and simulation of a lithium-ion battery with a phase change material thermal management system for an electric scooter," Journal of Power Sources **128,** 292-307 (2004).

5. R. Kandasamy, X. Q. Wang, and A. S. Mujumdar, "Transient cooling of electronics using phase change material (PCM)-based heat sinks," Applied Thermal Engineering **28,** 1047-1057 (2008).

6. P. Gauche, and X. Weiran, "Modeling phase change material in electronics using CFD - a case study," in *2000 International Conference on High-Density Interconnect and Systems Packaging*, 402-407 (2000).

7. S. Krishnan, and S. V. Garimella, "Analysis of a phase change energy storage system for pulsed power dissipation," IEEE Transactions on Components and Packaging Technologies **27,** 191-199 (2004).

8. S. Krishnan, J. Y. Murthy, and S. V. Garimella, "Analysis of solid-liquid phase change under pulsed heating," Journal of Heat Transfer-Transactions of the ASME **129,** 395-400 (2007).

9. D. W. Yoo, and Y. K. Joshi, "Energy efficient thermal management of electronic components using solid-liquid phase change materials," IEEE Transactions on Device and Materials Reliability **4,** 641-649 (2004).

10. T. Aldoss, D. J. Ewing, Y. Zhao, and L. Ma, "Numerical investigation of phase change materials for thermal management systems," SAE Technical Paper Series**,** (2009).

11. A. S. Fleischer, R. D. Weinstein, and T. Kopec, "Analysis of transient thermal management characteristics of PCM with an embedded carbon heat sink," in *The Tenth Intersociety Conference on Thermal and Thermomechanical Phenomena in Electronics Systems*, (2006), pp. 1265-1268.

12. S. T. Hong, and D. R. Herling, "Open-cell aluminum foams filled with phase change materials as compact heat sinks," Scripta Materialia **55,** 887-890 (2006).

13. P. A. E. Vallejos, and C. Duston, "Carbon foam filled with phase change materials for passive temperature management," in *COMSOL Multiphysics Users* (2005).

14. V. V. Kulish, and J. L. Lage, "Diffusion within a porous medium with randomly distributed heat sinks," International Journal of Heat and Mass Transfer **43,** 3481-3496 (2000).

15. S. Kirkpatrick, C. D. Gelatt Jr, and M. P. Vecchi, "Optimization by simulated annealing," Science **220,** 671-680 (1983).

16. M. Miki, T. Hiroyasu, J. Wako, and T. Yoshida, "Adaptive temperature schedule determined by genetic algorithm for parallel simulated annealing," in *The 2003 Congress Evolutionary Computation*, 459-466 (2003).

17. E. L. Piccolomini, and F. Zama, "The conjugate gradient regularization method in computed tomography problems," Applied Mathematics and Computation **102,** 87-99 (1999).

18. W. Cai, D. J. Ewing, and L. Ma, "Application of simulated annealing for multispectral tomography," Computer Physics Communications **179,** 250-255 (2008).

19. W. Cai, and L. Ma, "Applications of critical temperature in minimizing functions of continuous variables with simulated annealing algorithm," Computer Physics Communications **181,** 11-16 (2010).

20. A. Corana, M. Marchesi, C. Martini, and S. Ridella, "Minimizing multimodal functions of continuous variables with the “simulated annealing” algorithm," ACM Transactions on Mathematical Software (TOMS) **13,** 262-280 (1987).

21. L. Ma, and W. Cai, "Numerical investigation of hyperspectral tomography for simultaneous temperature and concentration imaging," Applied Optics **47,** 3751-3759 (2008).

22. L. Ma, W. Cai, A. W. Caswell, T. Kraetschmer, S. T. Sanders, S. Roy, and J. R. Gord, "Tomographic imaging of temperature and chemical species based on hyperspectral absorption spectroscopy," Optics Express **17,** 8602-8613 (2009).

23. W. H. Press, B. P. Flannery, S. A. Teukolsky, and W. T. Vetterling, *Numerical Recipes* (Cambridge University Press, 2007).

24. L. Ingber, "Very fast simulated re-annealing," Mathematical and Computer Modelling **12,** 967-973 (1989).

25. S. W. Mahfoud, and D. E. Goldberg, "Parallel recombinative simulated annealing: A genetic algorithm," Parallel Computing **21,** 1-28 (1995).

26. I. G. Tsoulos, and I. E. Lagaris, "Genanneal: Genetically modified simulated annealing," Computer Physics Communications **174,** 846-851 (2006).

27. A. Basu, and L. N. Frazer, "Rapid determination of the critical temperature in simulated annealing inversion," Science **249,** 1409-1412 (1990).

28. W. Ben-Ameur, "Computing the initial temperature of simulated annealing," Computational Optimization and Applications **29,** 369-385 (2004).

29. H. Cohn, and M. Fielding, "Simulated annealing: Searching for an optimal temperature schedule," SIAM Journal on Optimization **9,** 779-802 (1999).

30. M. Fielding, "Simulated annealing with an optimal fixed temperature," SIAM Journal on Optimization **11,** 289-307 (2000).

31. J. P. B. Leite, and B. H. V. Topping, "Parallel simulated annealing for structural optimization," Computers & Structures **73,** 545-564 (1999).

32. M. Miki, T. Hiroyasu, M. Kasai, K. Ono, and T. Jitta, "Temperature parallel simulated annealing with adaptive neighborhood for continuous optimization problem," International Journal of Computational Intelligence and Applications**,** 149-154 (2002).

33. A. Sohn, "Parallel n-ary speculative computation of simulated annealing," IEEE Transactions on Parallel and Distributed Systems **6,** 997-1005 (1995).

34. E. E. Witte, R. D. Chamberlain, and M. A. Franklin, "Parallel simulated annealing using speculative computation," IEEE Transactions on Parallel and Distributed Systems **2,** 483-494 (1991).

35. C. J. Geyer, and E. A. Thompson, "Annealing Markov chain Monte Carlo with applications to ancestral inference," Journal of the American Statistical Association **90,** 909-920 (1995).

36. U. H. E. Hansmann, "Effective way for determination of multicanonical weights," Physical Review E **56,** 6200-6203 (1997).

37. Y. Li, V. A. Protopopescu, N. Arnold, X. Zhang, and A. Gorin, "Hybrid parallel tempering and simulated annealing method," Applied Mathematics and Computation **212,** 216-228 (2009).

38. K. Kimura, and K. Taki, "Time-homogeneous parallel annealing algorithm," in *Proceedings of the 13th IMACS World Congress on Computation and Applied Mathematics*, (1991).

39. D. E. Goldberg, *Genetic Algorithms in Search, Optimization, and Machine Learning* (Addison-Wesley Reading, Menlo Park, 1989).

40. A. Sari, and K. Kaygusuz, "Thermal energy storage system using stearic acid as a phase change material," Solar Energy **71,** 365-376 (2001).

41. K. Cho, and M. Choi, "Experimental study on the application of paraffin slurry to high density electronic package cooling," Heat and Mass Transfer **36,** 29-36 (2000).

42. X. M. Fang, and Z. G. Zhang, "A novel montmorillonite-based composite phase change material and its applications in thermal storage building materials," Energy and Buildings **38,** 377-380 (2006).

43. Z. L. Liu, Z. Y. Wang, and C. F. Ma, "An experimental study on the heat transfer characteristics of a heat pipe heat exchanger with latent heat storage. Part II: simultaneous charging/discharging modes," Energy Conversion and Management **47,** 967-991 (2006).

44. I. O. Salyer, and A. K. Sircar, "A review of phase change materials research for thermal energy storage in heating and cooling applications at the University of Dayton from 1982 to 1996," International Journal of Global Energy Issues **9,** 183-198 (1997).

45. R. Akhilesh, A. Narasimhan, and C. Balaji, "Method to improve geometry for heat transfer enhancement in PCM composite heat sinks," International Journal of Heat and Mass Transfer **48,** 2759-2770 (2005).

46. R. H. Henze, and J. A. C. Humphrey, "Enhanced heat-conduction in phase-change thermal-energy storage devices," International Journal of Heat and Mass Transfer **24,** 459-474 (1981).

47. V. V. Calmidi, and R. L. Mahajan, "The effective thermal conductivity of high porosity fibrous metal foams," Journal of Heat Transfer **121,** 466-471 (1999).

48. Y. K. Joshi, and D. Pal, "Application of Phase Change Materials to Thermal Control of Electronic Modules: A Computational Study," in *Proceedings of the International Packaging Conference* **10,** (1995).

49. M. Kaviany, *Principles of Heat Transfer in Porous Media* (Pringer-Verlag, 1995).

50. A. D. Brent, V. R. Voller, and K. J. Reid, "Enthalpy-porosity technique for modeling convection-diffusion phase-change - application to the melting of a pure metal," Numerical Heat Transfer **13,** 297-318 (1988).

51. S. Patankar, *Numerical Heat Transfer and Fluid Flow* (Hemisphere, 1980).

52. K. Peippo, P. Kauranen, and P. D. Lund, "A multicomponent PCM wall optimized for passive solar heating," Energy and Buildings **17,** 259-270 (1991).

53. H. Zhao, and N. Ladommatos, "Optical diagnostics for soot and temperature measurement in diesel engines," Progress in Energy and Combustion Science **24,** 221-255 (1998).

54. M. C. Thurber, and R. K. Hanson, "Simultaneous imaging of temperature and mole fraction using acetone planar laser-induced fluorescence," Experiments in Fluids **30,** 93-101 (2001).

55. L. Ma, S. T. Sanders, J. B. Jeffries, and R. K. Hanson, "Monitoring and control of a pulse detonation engine using a diode-laser fuel concentration and temperature sensor," Proceedings of the Combustion Institute **29,** 161-166 (2003).

56. J. B. Swithenbank, J. M. Beer, D. S. Taylor, D. Abbot, and G. C. McCreath, "A laser diagnostic technique for the measurement of droplet and particle size distribution," in *14th AIAA Aerospace Sciences Meeting,* (1976).

57. W. D. Bachalo, and M. J. Houser, "Phase/doppler spray analyzer for simultaneous measurements of drop size and velocity distributions," Optical Engineering **23,** 583-590 (1984).

58. R. A. Dobbins, and G. S. Jizmagia, "Optical scattering cross sections for polydispersions of dielectric spheres," Journal of the Optical Society of America **56,** 1345-1349 (1966).

59. R. A. Dobbins, and G. S. Jizmagia, "Particle size measurements based on use of mean scattering cross sections," Journal of the Optical Society of America **56,** 1351-1352 (1966).

60. L. Ma, and R. K. Hanson, "Measurement of aerosol size distribution functions by wavelength-multiplexed laser extinction," Applied Physics B-Lasers and Optics **81,** 567-576 (2005).

61. L. A. Melton, A. M. Murray, and J. F. Verdieck, "Multiple parameter fuel spray analysis using Exciplex visualization: temperature, vapor/liquid concentrations, and oxygen pressure," in *Proceedings of the Combustion Institute*, (1985).

62. A. C. Chraplyvy, "Nonintrusive measurements of vapor concentrations inside sprays," Applied Optics **20,** 2620-2624 (1981).

63. J. M. Tishkoff, D. C. Hammond, and A. C. Chraplyvy, "Diagnostic measurements of fuel spray dispersion," Transactions of the ASME. Journal of Fluids Engineering **104,** 313-317 (1982).

64. T. C. Hanson, D. F. Davidson, and R. K. Hanson, "Shock tube measurements of water and n-dodecane droplet evaporation behind shock waves," in *Proceedings of the 43rd Aerospace Sciences Meeting*, **AIAA-2005-0350**, (2005).

65. T. C. Hanson, "The development of a facility and diagnostics for studying shock-induced behavior in micron-sized aerosols," Ph.D. Thesis, Stanford University, Stanford, CA.**,** (2005).

66. C. F. Bohren, and D. R. Huffman, *Absorption and Scattering of Light by Small Particles* (Wiley-Interscience, 1983).

67. N. C. Wickramasinghe, *Light Scattering Functions for Small Particles, with Applications in Astronomy* (Adam Hilger, 1991).

68. G. M. Hale, and M. R. Querry, "Optical constants of water in the 200-nm to 200-mu m wavelength region," Applied Optics **12,** 555-563 (1973).

69. L. Kou, D. Labrie, and P. Chylek, "Refractive indices of water and ice in the 0.65- to 2.5- μm spectral range," Applied Optics **32,** 3531-3540 (1993).

70. P. C. Ariessohn, S. A. Self, and R. H. Eustis, "Two-wavelength laser transmissometer for measurements of the mean size and concentration of coal ash droplets in combustion flows," Applied Optics **19,** 3775-3781 (1980).

71. N. L. Swanson, B.D. Billard, and T.L. Gennaro, "Limits of optical transmission measurements with application to particle sizing techniques," Applied Optics **38,** 5887-5893 (1999).

72. K. L. Cashdollar, C. K. Lee, and J. M. Singer, "Three-wavelength light transmission technique to measure smoke particle size and concentration," Applied Optics **18,** 1763-1769 (1979).

73. X. S. Cai, G. Zheng, and N. N. Wang, "A new dependent model for particle sizing with light extinction," Journal of Aerosol Science **26,** 685-688 (1995).

74. E. Winklhofer, and A. Plimon, "Monitoring of hydrocarbon fuel-air mixtures by means of a light extinction technique in optically accessed research engines," Optical Engineering **30,** 1262-1268 (1991).

75. K. Deb, and S. Agrawal, "Understanding interactions among genetic algorithm parameters," Foundations of Genetic Algorithms **5**, 265-286 (1999).

76. A. Kone, and D. A. Kofke, "Selection of temperature intervals for parallel-tempering simulations," The Journal of Chemical Physics **122,** 206101 (2005).

77. A. Schug, and W. Wenzel, "All-atom folding of the TRP-cage protein with an adpative parallel tempering method," Europhysics Letters **67,** 307 (2004).